Turbulent Transport Mechanism in the Roughness Sublayers over Idealized Urban Areas and its Implication to Street-Level Ventilation

Abstract

Turbulence in the roughness sublayer (RSL) is inhomogeneous compared with that in the inertial sublayer (ISL) of the atmospheric surface layer (ASL) over urban areas. Drag coefficient C_d, which measures aerodynamic roughness, is employed in this paper to examine how (idealized) urban morphology influences ASL dynamics and transport. Wind tunnel experiments are conducted to study the flows and turbulence in response to different configurations of (identical) roughness elements. Statistics, quadrant analysis, and tilt angle evidence the more efficient RSL transport over rougher surfaces even the winds are slower. Although the power spectra of streamwise u'' and vertical w'' fluctuating velocities are rather insensitive to C_d, their cospectrum shows a secondary peak at small motion scales λ_x ($\leq 0.1\delta$ where δ is the thickness of turbulent boundary layer) along with the primary peak at integral length scale Λ_x ($\approx \delta$). It is thus suggested that, regardless of the turbulence intensity, RSL streamwise and vertical winds are more correlated, enhancing the transport. Amplitude (AM) and frequency (FM) modulations signify the positive correlation between RSL large and small motion scales which is amplified over rougher surfaces. Furthermore, RSL turbulence kinetic energy (TKE) production (entrainment) increases with decreasing (increasing) C_d, fostering the basic mechanism of street-level ventilation. (*Word Count:* 200)

Keywords: aerodynamic resistance; drag coefficient C_d; inertial sublayer (ISL); roughness sublayer (RSL); turbulent transport; ~~urban canopy layer (UCL);~~ wind tunnel experiment.

1. Introduction

Air pollution poses a serious health risk, causing 7 million premature deaths worldwide annually (Dhimal et al., 2021). In view of the dense population, the air quality in urban environment is one of the major public concerns, especially in rapidly growing cities (Lawal et al., 2023; Vidanapathirana et al., 2023). The layout of congested, high-rise buildings in mega cities further hinders pollutant dilution and removal from street level, degrading the urban air quality (Liang et al., 2023; Zhang et al., 2022). Therefore, it is crucial to advance our understanding of turbulent transport in the atmospheric surface layer (ASL) over urban areas in order to improve the living environment (Michioka et al., 2023).

Urban morphology largely influences the street-level ventilation and air quality (He et al., 2020; Leung et al., 2012; Lim et al., 2022; Peng et al., 2021). Evidently, surface roughness is one of the key factors governing the transport processes (Liu et al., 2015). A series of systematic studies have been conducted to examine how urban roughness affects street-level ventilation and pollutant removal (Liu et al., 2018). In short, surface roughness promotes pollutant removal yet the transport mechanism is unknown (Mo and Liu, 2019). In this connection, this study is conceived to extend our on-going research effort, elucidating the fundamental turbulent transport mechanism in terms of intermittent motion scales.

ASL, which consists of the inertial sublayer (ISL) and the roughness sublayer (RSL), develops over buildings and trees (sizeable roughness elements) on ground surface (Raupach et al., 1991). ISL is elevated high enough above the (urban or vegetation) canopy where the flows and turbulence are rather homogeneous so the classic Monin–Obukhov similarity theory (MOST) can be applied (Brunet, 2020). RSL, on the other hand, covers 2*h* to 5*h* over the surface-mounted roughness elements with characteristic height *h*. Different from its ISL counterpart, the turbulence within the RSL is modified by individual roughness elements that ends up with substantial spatial variation (Peng and Sun, 2014). In view of the dissimilar turbulence statistics, the transport processes in the turbulent boundary layers (TBLs) over rough walls are more efficient than those over smooth walls (Finnigan et al., 2009). It is noteworthy that flows are decelerating and turbulence kinetic energy (TKE) is diminishing toward a rougher surface yet the transport processes, both momentum and pollutant, are enhanced (Mo and Liu, 2018a). As such, there is a need for the in-depth understanding of the winds and turbulence structures in RSLs as well as the fundamental transport mechanism.

The turbulent transport efficiency in ISLs can be described in terms of drag coefficient

$$C_d = \frac{2u_\tau^2}{U_\infty^2} \tag{1}$$

where u_τ is the friction velocity and U_∞ the freestream wind speed (Liu et al. 2015). It indeed measures the efficiency of momentum transport which is positively correlated with that of turbulent transport. Different from open terrain, urban areas consist of sizeable roughness elements that exert substantial drag on the flows aloft, modifying various atmospheric processes (Barlow, 2014). The drag parameterization over rough surfaces, such as air-land or air-sea interaction, is a keen topic Most studies have simplified the existence of RSL, which, however, complicates the transport processes so the conventional ASL parameterization is not fully applicable to urban areas (Ho and Liu 2017).

Numerous studies have been directed toward the response of aerodynamic resistance with a range of building configuration and packing density. The effects of layout, winds, and height variability of building blocks on drag coefficient C_d were examined so as to formulate an urban aerodynamic parameter. Apart from plan area index λ_p and frontal area index λ_f (Hagishima et al., 2009; Li et al., 2022), the drag coefficient C_d is sensitive to the standard deviation of building height (σ_h; Zaki et al., 2011). However, these studies have only investigated C_d as an aerodynamic parameter being influenced by urban surfaces but not the transport mechanism. Focusing on the turbulent flows over dense urban area, Peng and Sun (2014) suggested that the drag coefficient is independent from wind speeds. Recently, Yuan and Aghaei Jouybari (2018) found that drag coefficient is able to determine the double-averaged momentum flux, form-drag-induced shear, as well as turbulence production in RSLs. Besides, Mo and Liu (2018b) revealed that rougher urban surfaces increase aerodynamic resistance that in turn enhance street-level ventilation. Lately, Shao et al., (2022) proved that the drag coefficient is positively correlated with the coherent turbulence structures. These findings have outlined the interaction among drag coefficients, urban morphology, and turbulent transport. However, there is still a lack of systematic investigation or theoretical evidence for the mechanism behind the RSL transport over urban areas using drag coefficients.

Over the decades, it has been recognized that the turbulence characteristics in the ISL above vegetation canopies differ much from those in the RSL (Belcher et al., 2012). Fitzmaurice et al. (2004) used large-eddy simulation (LES) to calculate the neutrally stratified flows in and immediately above a vegetation canopy. It was shown that the RSL mean-wind-speed profile possesses an inflection (significant shear) in the vicinity of the roughness elements. Finnigan et al. (2009) proposed a phenomenological model to differentiate the turbulence in the RSLs and ISLs over vegetation canopies using LES. Although heterogeneous, several studies have concurred that RSL turbulence is more coherent than the ISL one (Conan et al., 2015; Finnigan et al., 2009). Moreover, it is dominated by energetic eddies which govern the RSL transport of mass and momentum (Böhm et al., 2013; Finnigan and Shaw, 2000; Katul et al., 2006). How this energetic turbulence coherence drives RSL transport is our inquisitiveness.

In recent years, the interaction among the broad spectra of flows has been a major topic attracted numerous investigations (Chen and Vassilicos, 2022; Liu et al., 2023a; Mäteling et al., 2020; Pathikonda and Christensen, 2017; Perret and Kerhervé, 2019). Energy spectra of velocity fluctuation and momentum flux are essential to scale interaction. The dominant frequencies signify the spatio-temporal scales of eddy-resolved flows (Demarco et al., 2022). Power spectrum and cospectrum delineate how energy is distributed across eddies of different sizes using the fast Fourier transform (FFT; Roth et al., 2015). Apart from the primary spectral peak attributed to buildings, Liu et al. (2023b) used wavelet analysis to unveil a secondary peak, denoting the footprints of ~~very~~ large-scale motions (~~V~~LSMs) over real urban morphology. Alternatively, a data-driven approach to energy spectrum is the Hilbert-Huang transform (HHT). Wei et al. (2016) applied the Hilbert spectral analysis to characterize ASL turbulence scales. Agostini and Leschziner (2016) introduced the empirical mode decomposition (EMD) to investigate the inner-outer-scale interaction. Although scale interaction has been extensively studied, most of the existing studies in the literature were based on either smooth walls or arrays of identical, idealized roughness elements. There were few studies focusing on non-uniform surface roughness to investigate how different aerodynamic roughness, such as the drag coefficient and roughness length, influences the scale interaction.

As an extended effort of the previous investigations, the purposes of this study are to:

- Unveil the RSL transport mechanism in response to the more uniform mean winds;
- Examine how the aerodynamic resistance modifies the RSL transport and mixing; and
- Elucidate the RSL transport efficiency by statistical (time domain) and spectral (frequency domain) analyses.

This study examines the turbulent transport mechanisms near rough surfaces by signal processing to investigate how different motion scales contribute at different levels of aerodynamic resistance. For example, a low-pass filter, which is the most well received practical approach to decompose fluctuating signals, is applied to separate the motion scales. Energy spectra and amplitude modulation (AM) are introduced to contrast the contribution from different scales and their interactions. The TKE budget is used to compare the TKE production and turbulent entrainment (from ISL downward to RSL) over different rough surfaces.

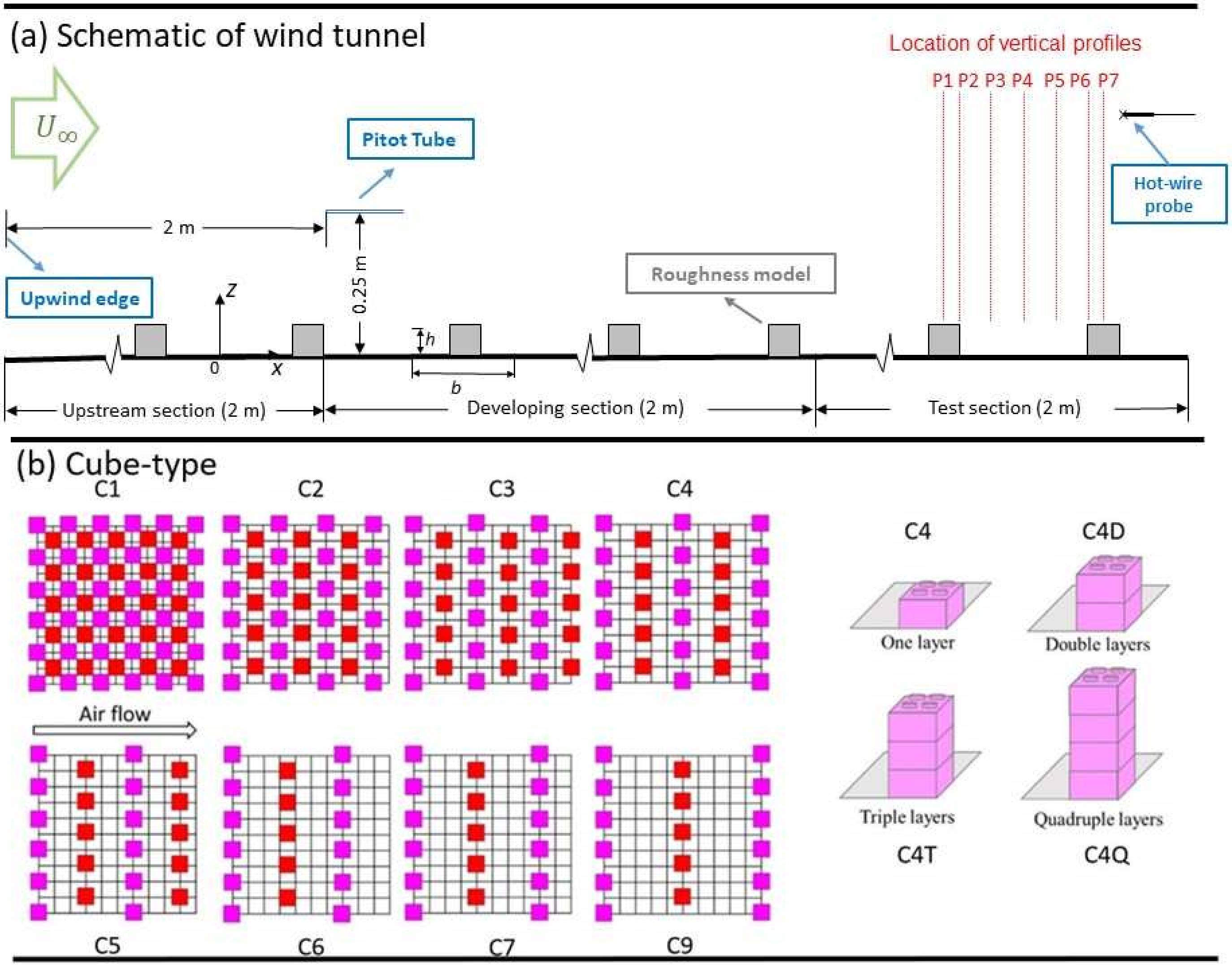

Figure 1. Configurations of cube-type, surface-mounted roughness elements employed in the wind tunnel experiments.

130

2. Methodology

2.1 Wind Tunnel Infrastructure

The experiments are conducted in the isothermal, open-circuit wind tunnel at the Department of Mechanical Engineering, The University of Hong Kong. The flows are driven by a centrifugal fan whose power is controlled by a frequency inverter (design wind speeds 0.5 m sec^{-1} $\leq U_0 \leq$ 15 m sec^{-1} in the empty test section). After the fan, a diffuser, a settling chamber, a flow straightener, and a contraction cone are built (in series) to control wind speed and turbulence level. Moreover, a honeycomb filter is installed after the flow straightener in-between the settling chamber and the contraction cone to reduce the background turbulence intensity ($\leq$ 5%). For environmental fluid mechanics applications, roughness elements are purposely added upstream the test section to modulate the mean-wind-speed profile and the turbulence intensity. The test section is made of acrylic whose dimensions are 6-m long × 0.56-m wide × 0.56-m high. The roughness elements, which are used to model idealized urban areas, are glued on the entire 6-m wind-tunnel floor to facilitate fully developed TBL flows. The details of our wind tunnel infrastructure are available elsewhere (Mo and Liu, 2018c).

The idealized urban morphology in the wind tunnel experiments is fabricated by plastic LEGO® blocks of size h (= 9.6×10^{-3} m; cube-type elements; Figure 1a). Arrays of LEGO® bricks are distributed in a staggered pattern whose streamwise separation b is adjusted to modulate the surface roughness, covering the range of $h \leq b \leq 9h$ (cases C1 to C9). In addition, the height of roughness elements is increased by mounting double (C4D; h = 19.2×10^{-3} m), triple (C4T; h = 28.8×10^{-3} m), and quadruple (C4Q; h = 38.4×10^{-3} m) layers of LEGO® bricks in the C4 configuration to extend the drag coefficient by height variability (Figure 1b). This ends up with the limitation of our work that the roughness element is relatively large with respect to the wind tunnel height (close to 7%). When the TBL develops to a certain extent, it affects the freestream region, causing the pressure gradient in the freestream region to change more negative, leading to the mild freestream acceleration phenomenon. The mean wind speeds in the presence of roughness elements are being monitored by a Pitot tube upstream the test section that is over 8 m sec^{-1} throughout the experiments. The Reynolds number Re_∞ ($= U_\infty\delta/\nu$) based on the TBL thickness δ and the kinematic viscosity of air at room temperature ν is over 10^5 to minimize the molecular effect.

2.2 Measurement and Data Acquisition

The flows are probed by a hotwire constant-temperature anemometer (CTA) with a crosswire design to measure the streamwise u and vertical w velocity components. The sensing element of the probe consists of a pair of 5×10^{-6}-m-diameter, platinum-plated tungsten wires with 2×10^{-3}-m active length by copper electroplating. The included angle between the two wires is 100° (≥ 90°) that helps reduce the inaccuracy due to inadequate yaw response in elevated turbulence intensity in the near-wall region. Sensor positioning on the vertical centerplane (x-z at $y = 0$; where x, y, and z are the streamwise, spanwise, and vertical direction, respectively) of the test section is controlled by a digital traverse system (spatial resolution 1 mm) and the National Instruments (NI) motion controllers (PCI-7390). The analog CTA signal is digitalized by a 24-bit NI data acquisition module (NI 9239; offset error ±0.05% for analog input ±10.52 V) mounted in a NI CompactDAQ chassis (NI cDAQ-9188). The NI units are connected to a digital computer via a local area network (LAN) cable. The LabVIEW software is used to process the automatic data acquisition and conversion for the measurements. Seven vertical profiles are collected for each test of roughness-element configuration (Figure 1a), covering the top of roughness elements (P1 and P7), cavity top (P3, P4, and P5), leeward edge (P2), and windward edge (P6). Along each vertical profile, 96 to 101 sampling points are probed, ranging from the roughness element height $z = h$ to the wall-normal distance over the TBLs z = 350 mm. The sampling duration at each point is over 66 sec and the sampling frequency is 2 kHz. In addition, the sample size (over 2^{17} data at each sampling point) is sufficiently large so the measurement time for each LEGO®-array configuration is over 12 hours. The CTA calibration is traceable based on the universal calibration law of the Institute of Sound and Vibration Research (ISVR; Bruun, 1971). Its readings are also compared in-house with those monitored by a Pitot tube in which the uncertainty is within 3%, and the correlation coefficient is up to $R^2 = 0.9997$.

3. Results and Discussion

3.1 Turbulence Statistics

3.1.1 Boundary-Layer Parameters

The TBL thickness δ is defined at the wall-normal distance z where the spatio-temporal average of wind speed converges to 99% of the freestream one $\left.\langle\overline{u}\rangle\right|_{z=\delta} = 0.99U_\infty$. In this study, the average freestream wind speed in the TBL is in the range of 10 m sec$^{-1} \le U_\infty \le$ 11 m sec^{-1} for cube-type roughness elements (Table 1). Here, the overbar $\overline{\psi}$ and angle brackets $\langle\psi\rangle$ denote temporal and spatial averages, respectively.

The friction velocity u_τ (= $(-\langle \overline{u''w''} \rangle)^{1/2}$) is the appropriate characteristic velocity scale in the near-wall region (Mo and Liu, 2023). In wind tunnel experiments, the aerodynamic resistance is commonly estimated from the spatio-temporal average of vertical momentum flux $u''w''$ which is much larger than the viscous momentum flux $\nu \partial \langle \overline{u} \rangle / \partial z$ over the entire rough surface. It was found that the Reynolds shear stress in the ISL is approximately 25% less than the surface stress deduced from pressure-difference measurements (Cheng et al., 2007). It in turn underestimates the friction velocity. Nonetheless, it is practically acceptable to adopt the square root of maximum vertical turbulent momentum flux to determine the friction velocity in wind tunnel experiments because the aerodynamic resistance is dominated by form drag (rather than viscous shear) in the current study. Here, double prime ψ'' (= $\psi - \langle \overline{\psi} \rangle$) denotes the deviation from the spatio-temporal average. The rough-TBL parameters, including the drag coefficient C_d, the zero-plane displacement d, and the roughness length z_0, are used to compare the aerodynamic resistance of the various settings of idealized urban morphology adopted in this paper. Using u_τ as the slope, the roughness length z_0 and the zero-plane displacement d are then determined by the best fit of the spatio-temporal average of mean-wind-speed vertical profiles measured in the wind tunnel experiments to the theoretical logarithmic law of the wall (log-law) in the ISL (linear regression). The range of ISL is identified in the above comparison as well whose deviation is bounded at 10%. Subsequently, the RSL height is defined at the ISL bottom. Their uncertainty is thus comparable to that of wind-speed measurements, i.e., 3% (Mo et al., 2021).

Table 1. Wind tunnel parameters and TBL properties over idealized urban morphology.

Case	h	b	h/b	U_∞	u_τ	C_d	δ	d	z_0
	[$\times 10^{-3}$ m]	[$\times 10^{-3}$ m]		[m sec^{-1}]	[m sec^{-1}]	[$\times 10^{-3}$]	[$\times 10^{-3}$ m]	[$\times 10^{-3}$ m]	[$\times 10^{-3}$ m]
C1	9.6	16	0.6	10.0	0.42	3.6	135	5.2	0.02
C2	9.6	32	0.3	10.9	0.53	4.8	165	5.8	0.08
C3	9.6	48	0.2	10.8	0.54	4.9	165	5.3	0.09
C4	9.6	64	0.15	10.8	0.56	5.5	165	5.6	0.13
C5	9.6	80	0.12	10.6	0.54	5.2	160	5.4	0.11
C6	9.6	96	0.1	10.6	0.54	5.1	165	5.3	0.10
C7	9.6	112	0.086	10.6	0.53	5.0	160	5.0	0.09
C9	9.6	144	0.067	10.7	0.51	4.5	155	4.8	0.06
C4D	19.2	64	0.3	10.8	0.60	6.3	190	5.8	0.23
C4T	28.8	64	0.29	11.1	0.66	7.1	215	5.1	0.37
C4Q	38.4	64	0.6	11.2	0.70	7.9	219	3.6	0.52

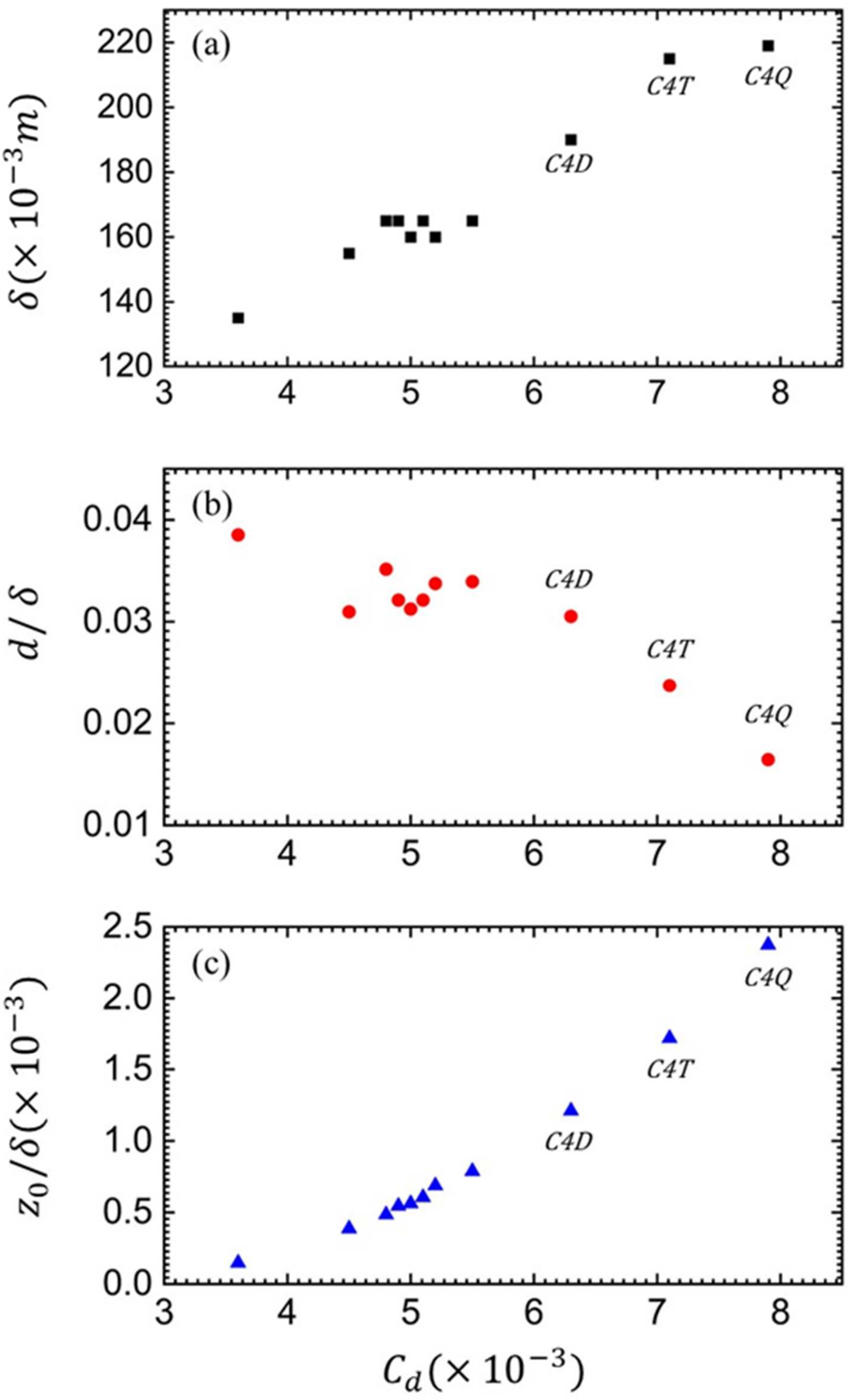

Figure 2. RSL parameters: (a) TBL thickness δ; (b) zero-plane displacement d; and (c) roughness length z_0 of the flows over cube-type roughness elements expressed in terms of drag coefficient C_d.

Figure 2 compares various aerodynamic parameters of the flows over different rough surfaces as functions of the drag coefficient C_d. In this study, the TBL thickness δ increases with increasing C_d (Figure 2a). It is because the TBL is (naturally) developed by the roughness elements. Whereas, the zero-plane displacement d does not show any notable correlation with the roughness elements tested (4.8×10^{-3} m $\leq d \leq 5.8\times10^{-3}$ m) except in the regime of high-drag coefficient ($C_d \approx 8\times10^{-3}$). In the cases C4D, C4T and C4Q, it drops sharply with increasing C_d (Figure 2b). As such, increasing roughness-element height h does not necessarily represent increasing zero-plane displacement d nor aerodynamic resistance C_d. On the other hand, roughness length z_0 increases monotonically with increasing C_d (Figure 2c). Its practical function as the measure of surface roughness is therefore concurred (Cheng et al., 2007).

3.1.2 Mean-Wind-Speed Profiles

The dimensionless profiles of the spatio-temporal average of mean-wind-speed $\langle \overline{u} \rangle / u_\tau$ over different idealized urban morphology collapse in the ISL (following the log-law) and the outer TBL (Figure 3). Apparently, the RSL mean-wind speeds are more uniform than their ISL counterparts, signifying the enhanced transport. ISL flows are rather homogeneous so the flux-gradient relationship can be applied in the form of the ~~Monin-Obukhov similarity theory (~~MOST~~)~~. Unlike the ISL, the dynamics in the RSL beneath is substantially modified by individual roughness elements. The RSL turbulent diffusivity was found enhanced (compared with that in the ISL) so the MOST is merely applicable. The log-law is no longer appliable to describe the RSL mean-wind speed, hence, an analytical solution was proposed specifically for both RSL and ISL winds elsewhere (Ho and Liu, 2017). In response to surface roughness, the mean-wind-speed profiles in the RSL shift downward with increasing drag coefficient C_d. Eventually, RSL flows are slowed down over rougher surfaces (yet the transport is enhanced).

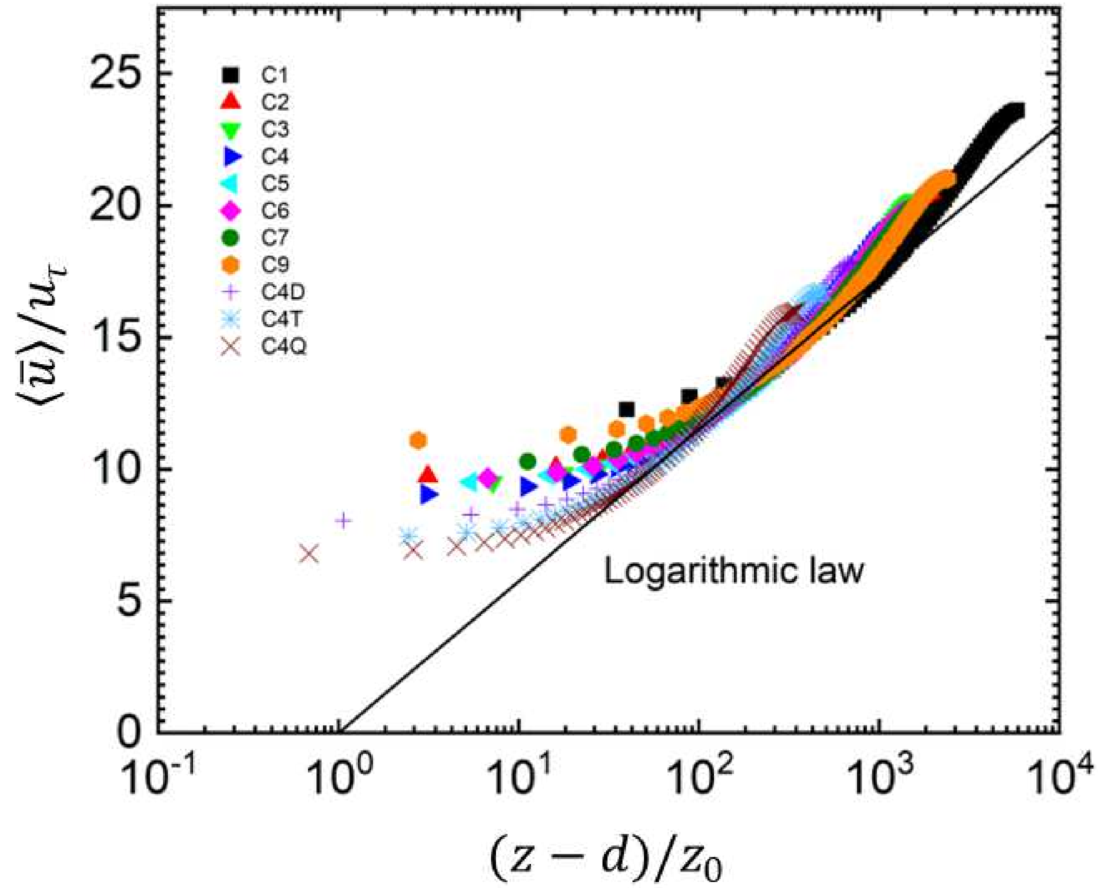

Figure 3. Dimensionless vertical profiles of spatio-temporal average of mean wind speed $\langle \bar{u} \rangle / u_\tau$ plotted against height $(z-d)/z_0$ in semi-logarithmic scale over idealized urban morphology.

3.1.3 Transport Efficiency

The momentum flux fraction

$$S_i = \frac{\left\langle \overline{u''w''} \right\rangle_{Qi}}{\left\langle \overline{u''w''} \right\rangle} \quad (2)$$

quantifies the contribution from the *i*-th quadrant *Qi* to the spatio-temporal average of vertical momentum flux $\left\langle \overline{u''w''} \right\rangle$. Subsequently, the exuberance

$$\eta = \frac{S_1 + S_3}{S_2 + S_4} \quad (3)$$

is defined to compare the transport efficiency over rough surfaces (Shaw et al., 1983). It is negative because S_1 and S_3 are larger than zero while S_2 and S_4 are smaller than zero. Moreover, less negative the exuberance implies more efficient the vertical transport. Quadrant events Q2 (ejection) and Q4 (sweep) signify the organized events that favor vertical momentum transport. On the contrary, quadrant events Q1 (outward interaction) and Q3 (inward interaction) represent the disordered events. Therefore, the closer the magnitude of η is to zero, the more coherent the events, i.e. more efficient the transport.

Previous studies have introduced the exuberance η to quantify the transport efficiency (Christen et al., 2007; Hertwig et al., 2017; Palusci et al., 2022). Yoshida et al. (2018) used this parameter to investigate the transport efficiency of vertical momentum flux that elucidated the relationship between building-height variability and characteristics of turbulent coherent structures. In effect, exuberance expresses the negative-to-positive-contributions ratio to momentum flux which indicates the vertical transport efficiency in terms of momentum. If the exuberance is close to zero, it is suggested that the (larger) downward transport dominates momentum and less unorganized, counter-flux events exist. It hence ends up with a more efficient transfer of momentum. It is noteworthy that the net momentum flux could be large even the exuberance is large in magnitude (i.e. inefficient transport). In this connection, comparing the vertical profiles of momentum flux is an alternative to examine the transport efficiency over different roughness which was reported elsewhere (Ho and Liu 2017b).

Previous studies have focused on the relative contributions of Q2 (ejection) to Q4 (sweep) at building height $z = h$ (S_2/S_4). Alike this study, comparing S_2/S_4 for regular and staggered arrays showed that Q4 (sweep) dominates the dynamics over staggered arrays (Kanda ,2006). Similarly, the outdoor measurements based on reduced-scale models of regular cubical roughness elements in neutral stability found that the relative contributions from Q4 (sweep) are larger than those from Q2 (ejection) in all locations and at all heights (Roth et al., 2015). The effect of both organized and disordered events on the transport efficiency of different rough surfaces will be further discussed.

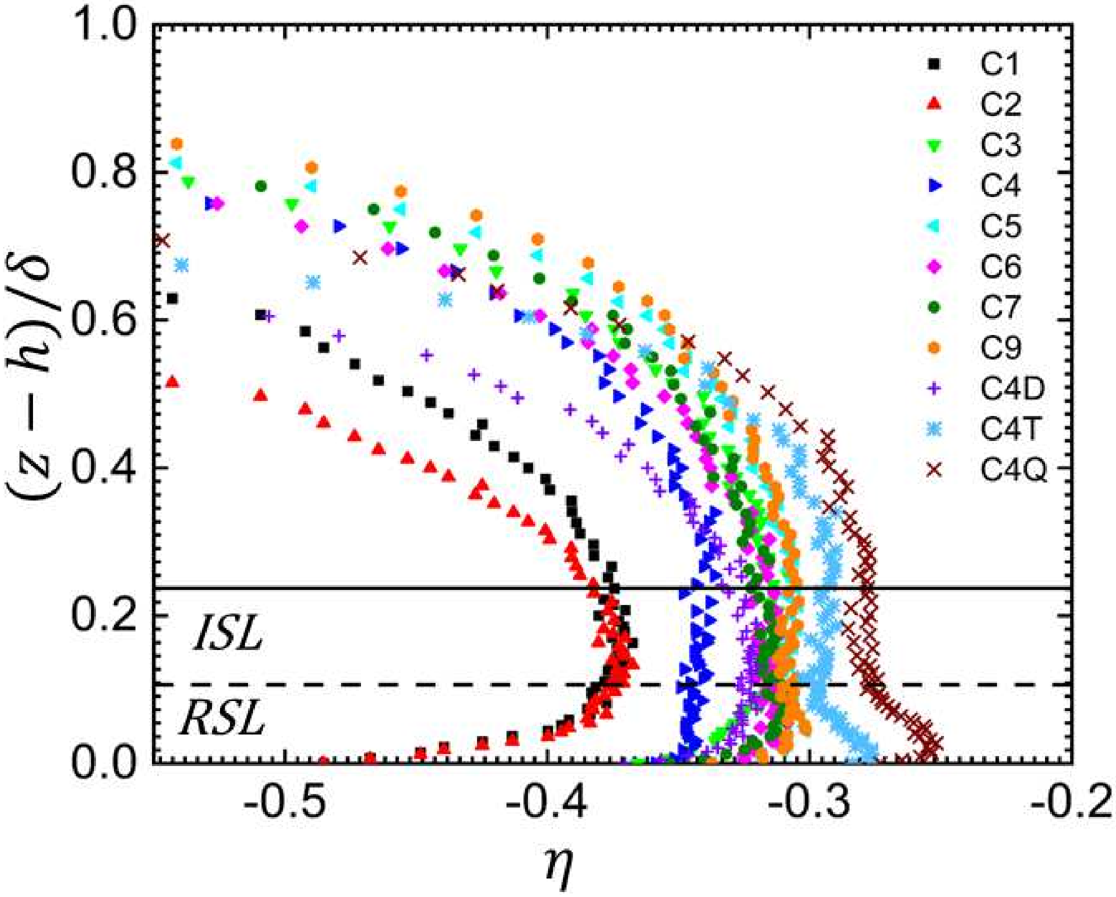

Figure 4. Vertical profiles of transport efficiency measured in terms of exuberance $\eta = (S_1 + S_3)/(S_2 + S_4)$. Dashed and solid lines denote the RSL and ISL top, respectively.

276

The exuberance η increases monotonically (less negative) with increasing drag coefficient C_d (Figure 4). In this connection, the transport efficiency gradually increases starting from the RSL bottom, arrives its (broad) maximum in the ISL, then decreases thereover toward the TBL top. Building height variability plays an important role in transport-efficiency improvement. In the cases C4T and C4Q (roughest), the transport efficiency increases sharply at the RSL bottom that outperforms its ISL counterpart, illustrating the roles of (dissimilar) buildings in urban ventilation. It is in turn implied that more diversified building height favors vertical transport in particular close to the urban canopy.

3.1.4 Tilt Angle

Quadrant analysis provides a perspective to examine turbulence structures. It divides the combination of streamwise and vertical flows into four quadrants on the $u'' - w''$ plane based on the sign (direction) of the fluctuating velocities. The quadrants are divided into outward interaction Q1 ($u'' > 0$ and $w'' > 0$), ejection Q2 ($u'' < 0$ and $w'' > 0$), inward interaction Q3 ($u'' < 0$ and $w'' < 0$), and sweep Q4 ($u'' > 0$ and $w'' < 0$). The joint probability density function (JPDF) $P(u'', w'')$ measures the occurrence frequency of streamwise u'' and vertical w'' fluctuating velocities. The product of JPDF and the vertical momentum flux $u''w''$ yields the covariance integral

$$\overline{u''w''} = \int_{-\infty}^{+\infty} u''w''P\left(u'', w''\right) du''dw'' \tag{4}$$

which is used to examine the composition of the total momentum flux. Applying JPDF found that low- and high-momentum structures are associated with Q2 (ejection) and Q4 (sweeps) of the flows, respectively (Michioka et al., 2011).

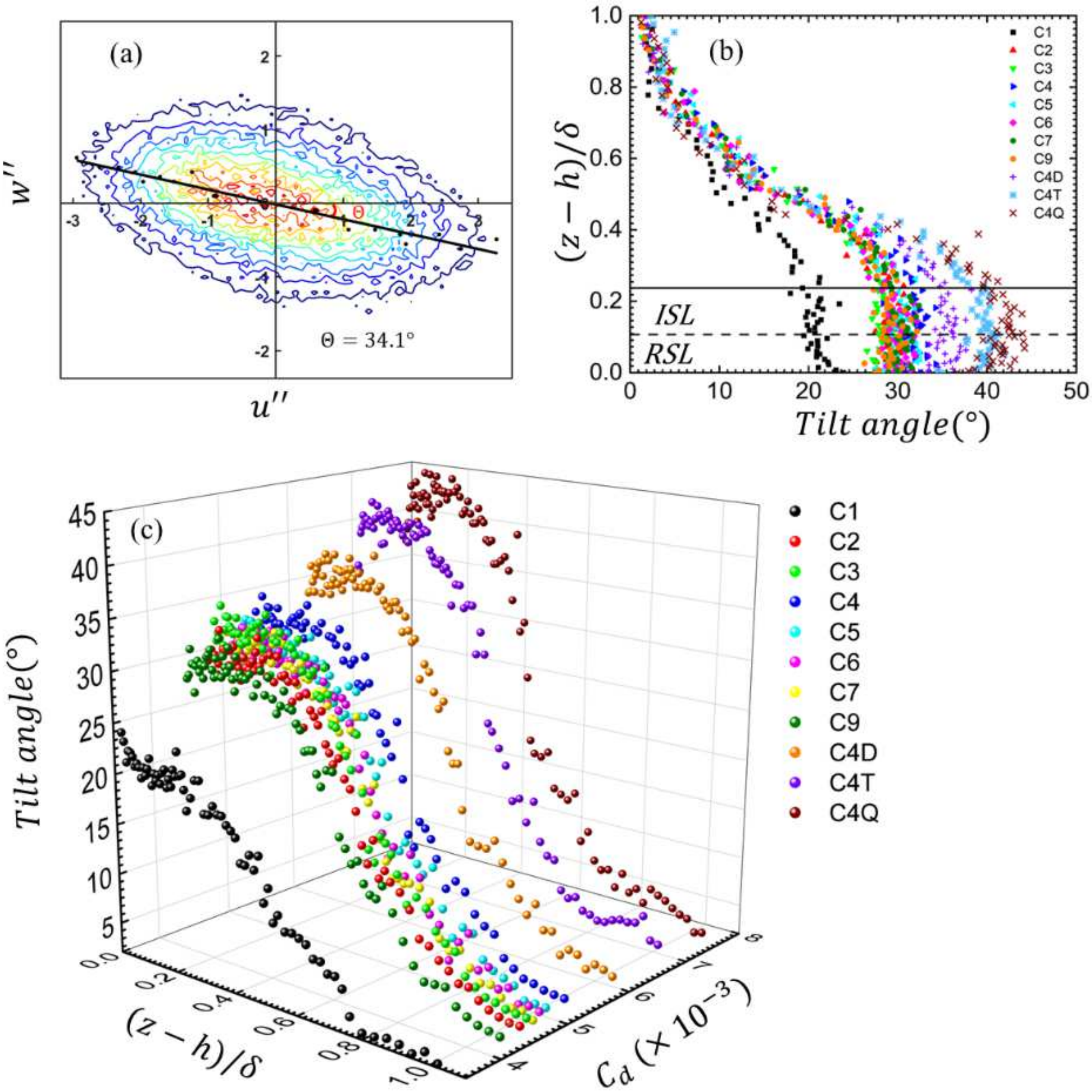

Figure 5. (a) Contours of joint probability density function (JPDF) of the streamwise and vertical fluctuating velocities $P(u'', w'')$ and the linear regression for the determination of the tilt angle Θ in Case C4. (b) Vertical profiles of the spatio-temporal average of tilt angle $\langle\overline{\Theta}\rangle$ over different configurations of cube-type roughness elements. (c) The spatio-temporal average of tilt angle $\langle\overline{\Theta}\rangle$ plotted as a function of drag coefficient C_d and height $(z - h)/\delta$. Dashed and solid lines denote the RSL and ISL top, respectively.

298 The tilt angle Θ is obtained by the linear regression of the most energetic Q2 and Q4 events on the JPDF (Figure 5a). The turbulence is isotropic when the tilt angle equals 45°. As

the tilt angle continues to increase, the vertical fluctuating velocity w'' increases to a greater extent than does the streamwise one u''. It is thus implied that the (vertical) transport is growing to be more energetic.

Figure 5b depicts the vertical profiles of the spatio-temporal average of the tilt angle $\langle \overline{\Theta} \rangle$ over different configurations of roughness elements. It is shown that, in the RSL, the tilt angle increases with height that is peaked roughly at the RSL-ISL interface (most efficient vertical transport). Apparently, there is a change in peaked tilt angle in response to drag coefficients C_d. At the same height, the tilt angle increases with increasing drag coefficient. Figure 5c shows this phenomenon more noticeably. Therefore, it is concluded that the ASL vertical fluctuating velocity w'' is more energetic over rougher surfaces. The tilt angle gradually decreases with increasing height in the ISLs. Thereover in the outer layer, it converges regardless of the drag coefficient. In this connection, the turbulence structure in the outer layer is merely influenced by surface roughness.

The above analysis suggests that the drag coefficient C_d is positively correlated to the transport efficiency (exuberance) η and the tilt angle Θ. Organized events (Q2 and Q4) possess more energetic vertical fluctuating velocity over rougher surfaces that favor ventilation. Hence, the following sections explore their interaction in order to elucidate the transport mechanism over urban areas. The augmented transport efficiency extends slightly over ISL to $0.5\delta \leq z \leq 0.8\delta$ that signifies the influence of surface-mounted roughness elements on the entire ASL.

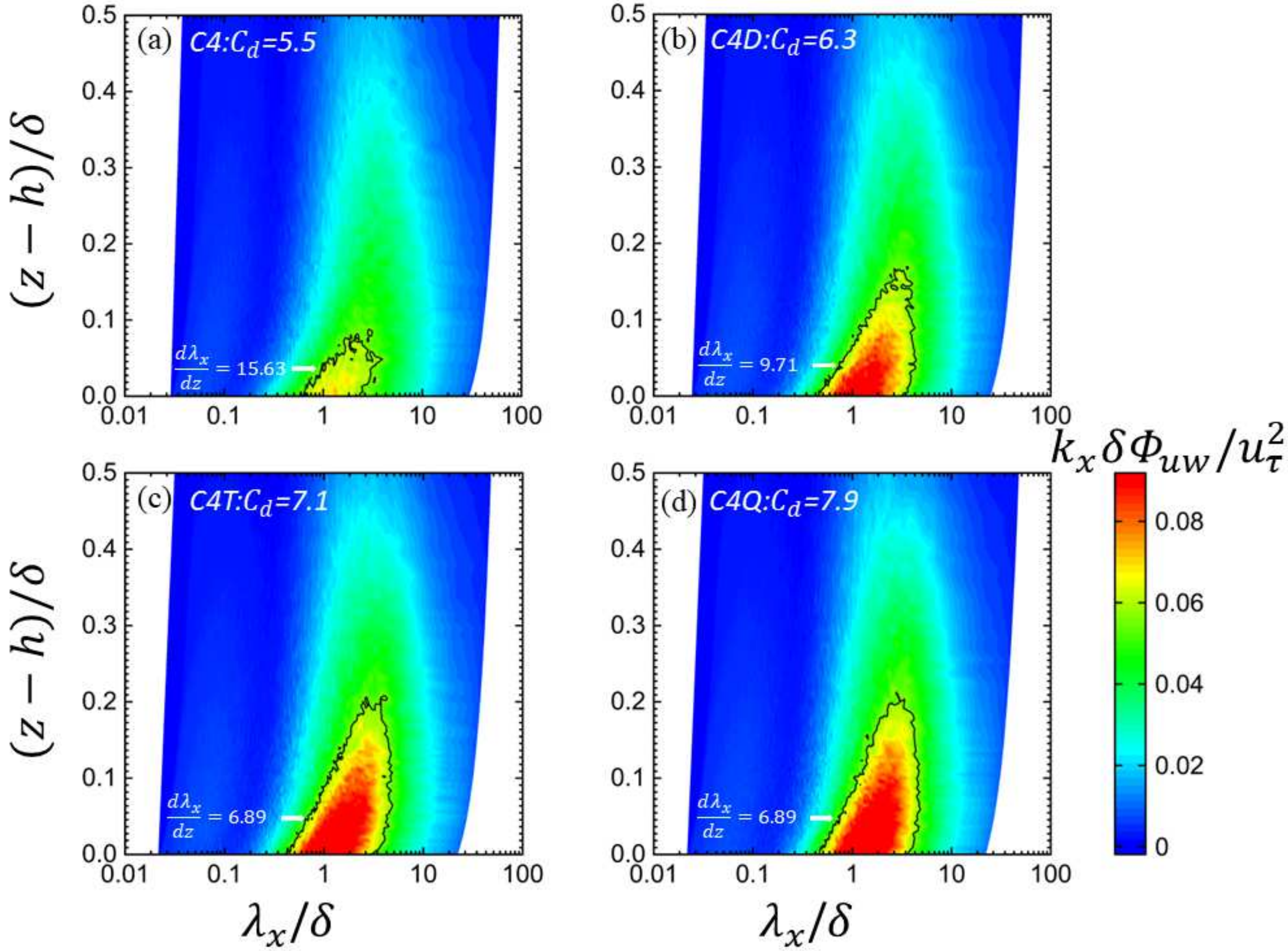

Figure 6. Shaded contours of dimensionless pre-multiplied energy cospectrum of the streamwise and vertical fluctuating velocities $k_x\delta\Phi_{uw}/u_\tau^2$ plotted as functions of motion scale λ_x/δ and height $(z-h)/\delta$. Cases (a) C4; (b) C4D; (c) C4T; and (d) C4Q.

321

3.2 Spectral Analysis

3.2.1 Energy Spectrum

Figure 6 compares the pre-multiplied energy cospectra of streamwise *u''* and vertical *w''* fluctuating velocities across the entire TBL to observe the energy distribution of the large- and small-scale structures. The streamwise Φ_{uu}/u_τ^2 and vertical Φ_{ww}/u_τ^2 energy spectra are non-dimensionalized by the friction velocity u_τ. Here, k_x (= $2\pi f_S \big/ \langle \overline{u} \rangle$) is the streamwise wavenumber based on the Taylor's frozen turbulence hypothesis that is calculated by the (sampling) frequency f_S and the ensemble average of mean-wind speed $\langle \overline{u} \rangle$ (Chin et al., 2009). Obviously, the integral length scale Λ_x, i.e., the scale of the peaked pre-multiplied energy cospectra, is comparable to the TBL thickness δ. It increases with increasing elevation as well.

The RSL motion scales are examined by frequency spectrum. Aerodynamic resistance also affects the dominant scale significantly. Comparing the cases C4, C4D, C4T, and C4Q with elevated C_d, it is noticeable that the vertical gradient of streamwise wavelength $d\lambda_x/dz$, which measures the change of the size of motion scales in height, decreases with increasing C_d (Figure 6). Moreover, the energy intensity increases with increasing aerodynamic resistance. Hence, the smoother the surface is, the faster the rate at which the dominant eddy size increases with increasing height in RSL and the lower the energy intensity. In other words, near-ground eddies are less heterogeneous over rougher surfaces.

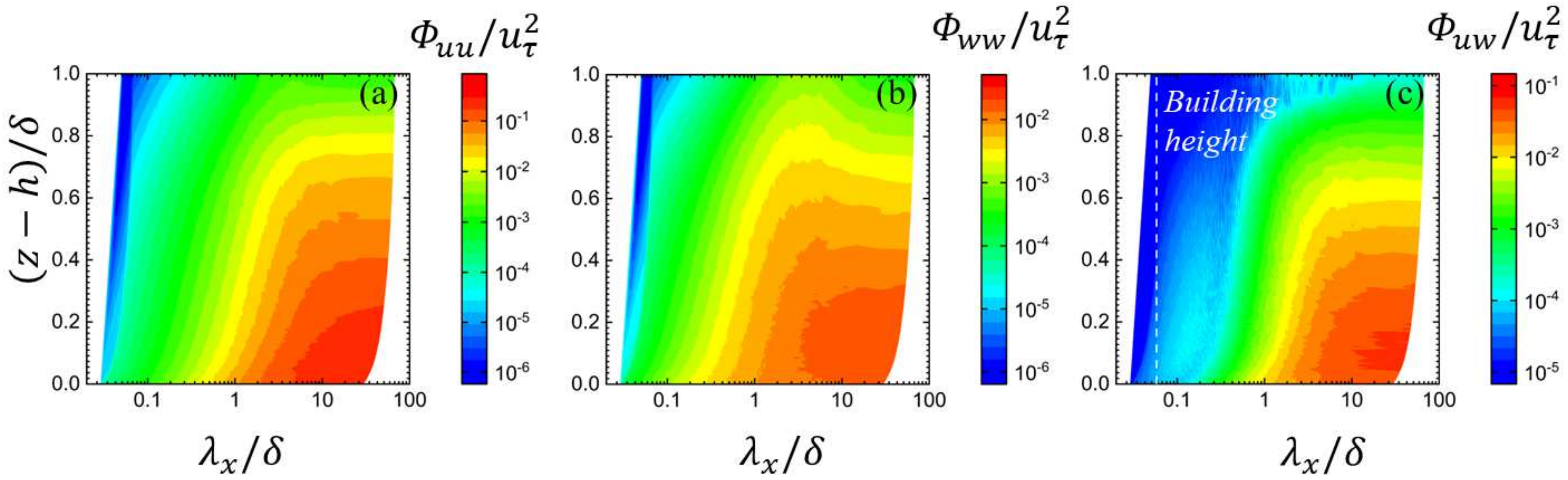

Figure 7. Shaded contours of dimensionless energy spectra in Case C4. (a) streamwise Φ_{uu}/u_τ^2 and (b) vertical Φ_{ww}/u_τ^2 fluctuating velocities together with (c) their cospectra Φ_{uw}/u_τ^2 plotted as functions of motion scale λ_x/δ and height $(z-h)/\delta$.

Using the roughness configuration setting C4 as an example (Figure 7), apparently, there is a peak in the power spectra and cospectra of streamwise u'' and vertical w'' fluctuating velocities. The peak is located approximately at $\lambda_x = 10\delta$ regardless of the elevation. Moreover, the streamwise motion scales obviously convey much more energy than the vertical ones (by almost an order of magnitude). As such, the energy is dominated by the anisotropic LSMs.

A secondary peak of cospectrum, whose wavelength λ_x is of the same order of magnitude of the building height h, is unexpectedly found in the logarithmic region that is attributed to small-scale motions roughly at $\lambda_x = 0.1\delta$ (Figure 7c). In particular, this sub-peak is not found in the power spectra of both streamwise and vertical fluctuating velocities. It is thus implied that, other than the integral length scale, TKE does not show any local maximum in the short-wavelength regime. Therefore, the small-scale motions ($\lambda_x < 0.1\delta$) are barely initiated by the roughness elements. Instead, the dynamics and intermittency are suppressed by the roughness elements while approaching the solid boundary. Under this circumstance, the secondary peak of cospectrum suggests that the streamwise and vertical fluctuating velocities are more correlated with each other in the RSL. As a result, the drag over rough surfaces enhances the mixing and transport processes.

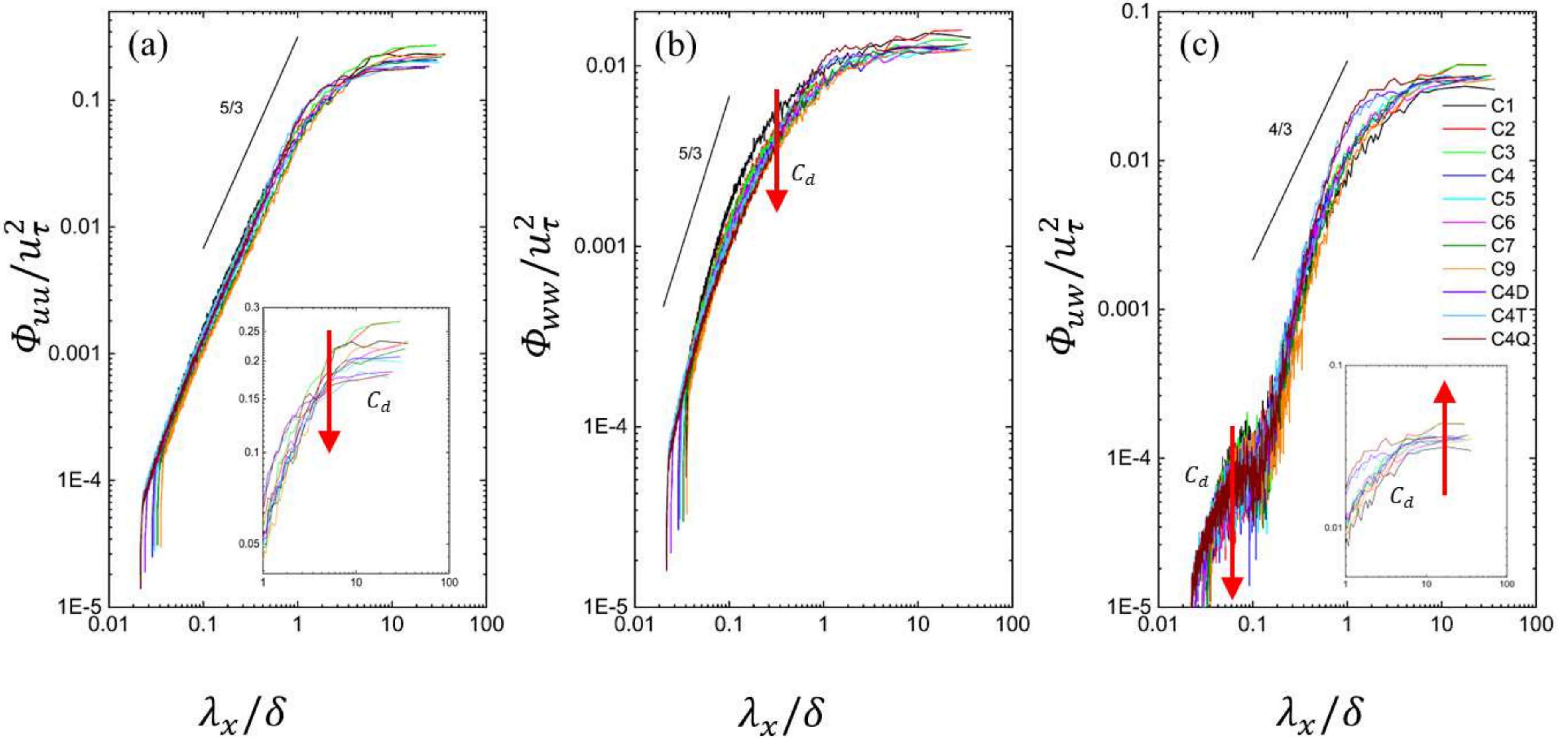

Figure 8. Energy spectra of the (a) streamwise Φ_{uu}/u_τ^2 and (b) vertical Φ_{ww}/u_τ^2 fluctuating velocities together with (c) the cospectra Φ_{uw}/u_τ^2 of u'' and w'' plotted as functions of motion scale λ_x/δ at $(z-h)/\delta = 0$. Arrow points increasing drag coefficient C_d.

360

Figure 8 compares the spectral energy density at the RSL bottom $z = h$ of all the cases. The energy density follows the conventional energy spectrum based on Kolmogorov's theory (Kolmogorov, 1991). For instance, the power spectra of both streamwise u'' and vertical w'' fluctuating velocities follow the −5⁄3 power-law scaling in the inertial subrange. In addition, a 4/3 ratio between the cospectral density of u'' and w'' follows as a consequence of local isotropy.

Compared with the long-wavelength region ($\lambda_x > \delta$), the energy spectra of streamwise u'' fluctuating velocities are smaller and are comparable over different rough surfaces in the shorter-wavelength regime ($\lambda_x < 0.1\delta$). It is thus suggested that the motions governing energy cascade and even dissipation are about the same scale regardless of the aerodynamic resistance in the dimensionless manner. On the contrary, a noticeable difference in the energy spectra is observed in the longer-wavelength regime. The spectra of both the streamwise (Figure 8a) and vertical (Figure 8b) fluctuating velocities grow in energy contents with decreasing drag coefficient. The spectral energy of w'' decreases with increasing C_d throughout the entire range of wavelength. On the other hand, the corresponding changes in u'' is limited in the long-wavelength region.

Sub-peaks with smaller motion scales are found in the cospectra between streamwise u'' and vertical w'' fluctuating velocities regardless of the surface roughness (Figure 8c). In the short-wavelength regime, a notable difference in the cospectra is observed among the rough surfaces with different C_d. The flows over the least rough surface (case C1) exhibit the highest sub-peak. The growth in the cospectral energy contents with decreasing drag coefficient in the short-wavelength regime signifies the tightly coupled (small-scale) streamwise *u''* and vertical *w''* fluctuating velocities in the RSLs. However, this phenomenon is reversed in the long-wavelength region, where the energy increases with increasing C_d. This finding is consistent with the previous discussion using the pre-multiplied energy spectrum (Figure 6). Therefore, the more uniform RSL turbulence transport processes are attributed to the large, energy-carrying motion scales together with the small, more correlated motion scales.

3.2.2 Isotropy

Statistical indicators are necessary to measure the interactions among motion scales. In particular, different scale ranges are characterized by varying the levels of energy-density anisotropy (Agostini and Leschziner, 2017) by the isotropy parameter

$$\gamma = \frac{2\left|\Phi_{uu}\right|\left|\Phi_{ww}\right|}{\left|\Phi_{uu}\right|^2 + \left|\Phi_{ww}\right|^2} \quad (5)$$

that tends to a maximum of unity in case of isotropy.

The RSL turbulence tends to be more anisotropic when it is approaching the rough surface (Figure 9). It implies that, though the eddies are large, they are isotropic when the height is over the ISL. However, the RSL eddies tend to be anisotropic even they are already small in size. This finding is consistent with our observations in the cospectra. As C_d increases, ~~the shorter is~~ the range of isotropic eddy size in the RSL is shortened. In the long-wavelength region, the isotropic tendency grows with increasing drag coefficient. It means that RSL large-scale structure over rougher surfaces is more isotropic than that over smoother surfaces. This finding is in line with the observation of tilt angle as well as previous study (Shafi and Antonia, 1997).

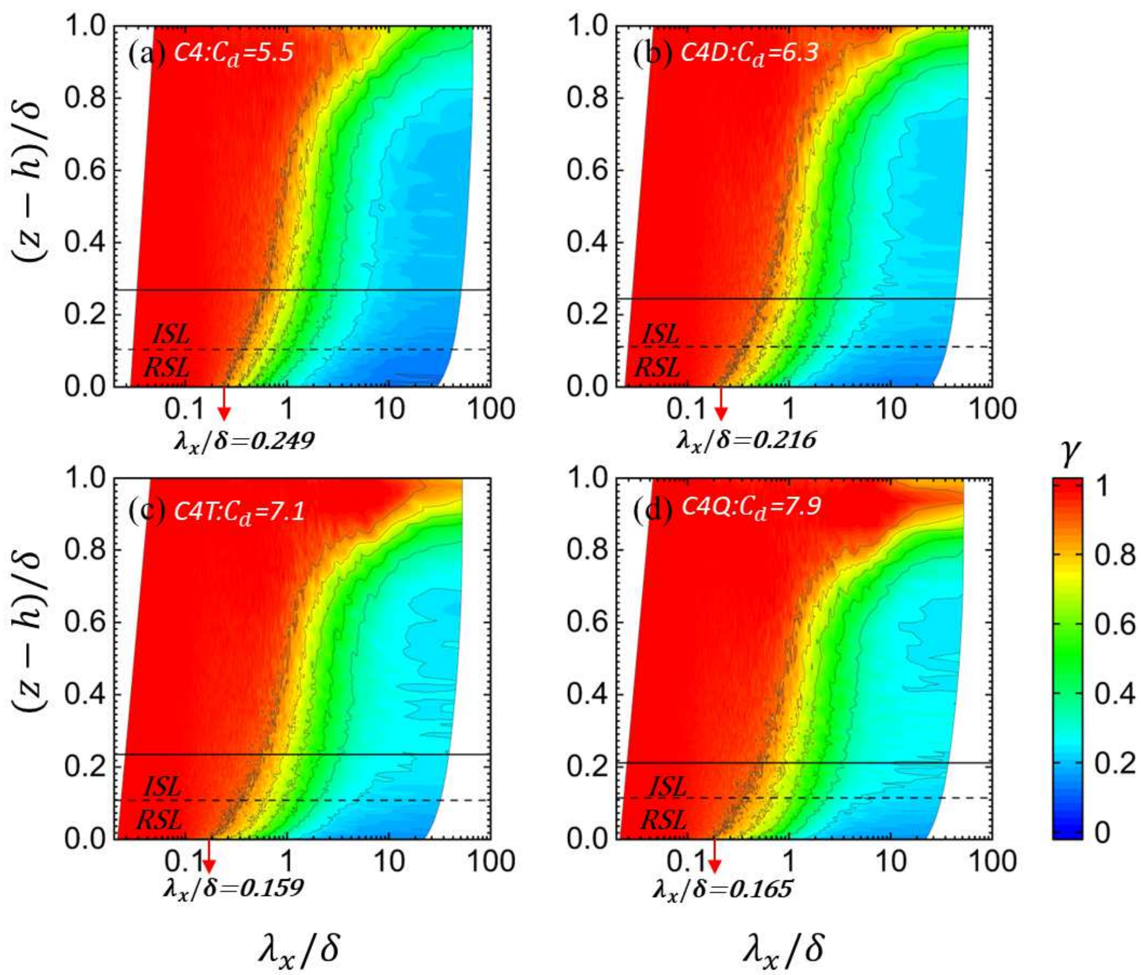

Figure 9. Shaded contours of isotropy parameter γ as functions of motion scale λ_x/δ and height $(z - h)/\delta$. Cases (a) C4; (b) C4D; (c) C4T; and (d) C4Q. Red arrows indicate λ_x/δ at which $\gamma = 0.875$.

406

3.2.3 TKE Budget

The effect of surface roughness on the TKE budget is important to elucidate the energy transfer within TBLs (Blackman et al., 2017). Numerous researches have attempted the TKE budget and fluxes (Yuan and Aghaei Jouybari, 2018).

To interpret the transport mechanism in RSLs, spectral analysis of TKE production is introduced (Cheng et al., 2020). TKE budget was derived by Lumley and Panofsky (1964),

$$\frac{\partial E(k_x)}{\partial t}+\frac{\partial Q(k_x)}{\partial z}=S(k_x)\frac{\partial\langle\overline{u}\rangle}{\partial z}-\frac{\partial\varepsilon(k_x)}{\partial k}+B(k_x)-2\nu k_x^2E(k_x) \tag{6}$$

where $E(k_x)$ is the spectral TKE density, $\partial Q(k_x)/\partial z$ the vertical TKE transfer in physical space, $S(k_x)$ the cospectrum of vertical momentum flux $u''w''$, $S(k_x)\times\partial\langle\overline{u}\rangle/\partial z$ the TKE transfer from mean flow to turbulence, $\varepsilon(k_x)$ the net rate of spectral energy transfer, and $2\nu k_x^2E(k_x)$ the TKE dissipation rate by molecular (kinematic) viscosity ν.

Figure 10 shows the shaded contours of the spectral TKE production $S(k_x)\times\partial\langle\overline{u}\rangle/\partial z$ as functions of streamwise wavelength λ_x and height $(z-h)$. Although it is the same peaked at large motion scales $\lambda_x = 10\delta$, the energy production decreases significantly with increasing aerodynamic resistance. It is therefore hypothesize that, as drag coefficient C_d increases, TKE production decreases but the entrainment (to RSL) increases. This practically means that rougher the surface is, the less TKE being produced but the more entrainment, and vice versa.

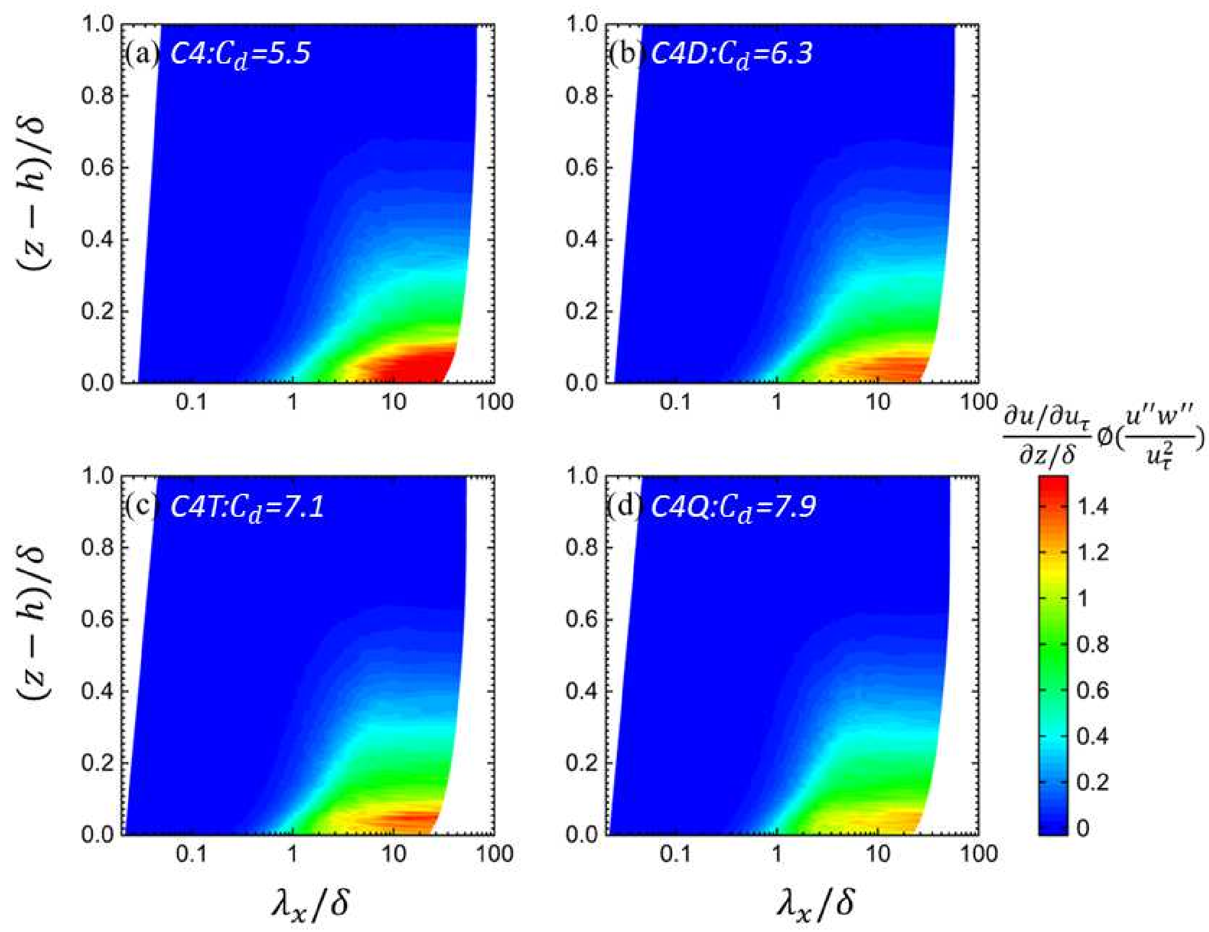

Figure 10. Shaded contours of spectral TKE production $S(k_x)\times\partial\langle\overline{u}\rangle/\partial z$ plotted as functions of wavelength λ_x/δ and height $(z-h)/\delta$. Cases (a) C4; (b) C4D; (c) C4T; and (d) C4Q.

425

3.3 Scale Interaction

3.3.1 Amplitude Modulation and Frequency Modulation

The scale interactions in the TBLs are examined to further characterize RSL turbulent transport. As shown in the pre-multiplied energy spectra (Figure 6), there is no notable high-energy peak at which the streamwise wavelength λ_x is much longer than inner peak representing very large-scale motions (VLSMs) in the outer layer (Tang et. al., 2016). Nevertheless, it is necessary to separate the raw fluctuating signals into the large- and small-scale components by a cut-off (wavelength) filter (Zhang et al., 2020). Alike previous studies, the cut-off wavelength $\lambda_x = \delta$ is selected from the pre-multiplied energy spectra that is essentially based on the integral length scale Λ_x.

Amplitude modulation (AM) and frequency modulation (FM) have been adopted to investigate the coupling between the small- and large-scale fluctuating velocities (Iacobello et al., 2021). The AM of TBL fluctuating flows is handled by the Hilbert transform (Mathis et al. 2009). Figure 11 depicts the representative filtered time traces of the raw data u'' at the roof level $(z - h)/\delta = 0$ over the case C4 (Figure 11a). The small-scale u_S'' (Figure 11b) and large-scale u_L'' (Figure 11c) fluctuating velocities are separated at wavelength $\lambda_x = \delta$. The filtered envelope $E_L(u_S'')$ is calculated by the Hilbert transform that describes the modulation of small-scale structures (Figure 11d). AM coefficient

$$R_{AM} = \frac{\overline{u_L'' E_L(u_S'')}}{\sqrt{\overline{u_L''^2}} \times \sqrt{\overline{E_L(u_S'')^2}}} \tag{7}$$

defines the correlation between the large-scale streamwise fluctuating velocity u_L'' and the filtered envelope of the small-scale fluctuating velocity $E_L(u_s'')$.

Similar to AM, the effect of FM between large and small scales is found in the RSL. Recently, Baars et al. (2015) adopted the continuous wavelet transform (CWT) to quantify the FM in wall-bounded turbulence. By convoluting the time series of streamwise fluctuating velocity $u''(t)$ with a mother wavelet function $\psi(t/s)$, the CWT coefficient

$$\widetilde{u''}(t,s)=\frac{1}{\sqrt{s}}\int_{-\infty}^{+\infty}u''(t')\times\psi\left(\frac{t'-t}{s}\right)dt' \tag{8}$$

is calculated where s is the wavelet time scales. In this study, the analytic Morlet wavelet is used as the mother wavelet for the convolution Equation (8). By transforming the wavelet time scale s to the frequency scale f according to the central frequency of the wavelet specified by Morlet, the wavelet power spectrum (WPS) at time t is equal to the square of the modulus of the CWT coefficients

$$\tilde{\phi}(t,f)=\left|\widetilde{u''}(t,f)\right|^{2}. \tag{9}$$

The wavelet transform includes 1,024 linear spaced scales to resolve the frequency in the range of 5 Hz $\le f \le f_N$ where f_N ($=fs/2$) is the Nyquist frequency. Afterward, the time series of the energy spectrum of the small-scale streamwise fluctuating velocity

$$\varsigma_S(t)=\sqrt{\int_{f_C}^{f_N}\tilde{\phi}(t,f)\,df} \tag{10}$$

is obtained by integrating the WPS Equation (9) from the cut-off frequency f_C to f_N to delineate the contribution from the small scales ($\ge fc$). It can also be used to construct the large-scale variation in small-scale amplitude. A representative, small-scale-frequency signal is taken as its instantaneous frequency (IF)

$$F_S(t) = \frac{1}{\left[\varsigma_S(t)\right]^2} \times \int_{f_C}^{f_N} \tilde{\phi}(t,f) \times f \, df \tag{11}$$

which is the first spectral moment of the small-scale energy spectrum.

The fluctuating instantaneous frequency $F_S''(t)$ (= $F_S(t) - \overline{F}_S$) is calculated where $\overline{F}_S$ is the temporal average of characteristic frequency of the small scales. Analogous to AM, after the low-pass-filtering $\lambda_x > \delta$, the large-scale variation of small-scale frequency $F_{S,L}''$ is obtained (Figure 11e). The FM coefficient

$$R_{FM} = \frac{\overline{u_L'' F_{S,L}''}}{\sqrt{\overline{u_L''^2}} \times \sqrt{\overline{F_{S,L}''^2}}} \tag{12}$$

defines the correlation between the large-scale streamwise fluctuating velocity u_L'' and the large-scale variation of the small-scale frequency $F_{S,L}''$.

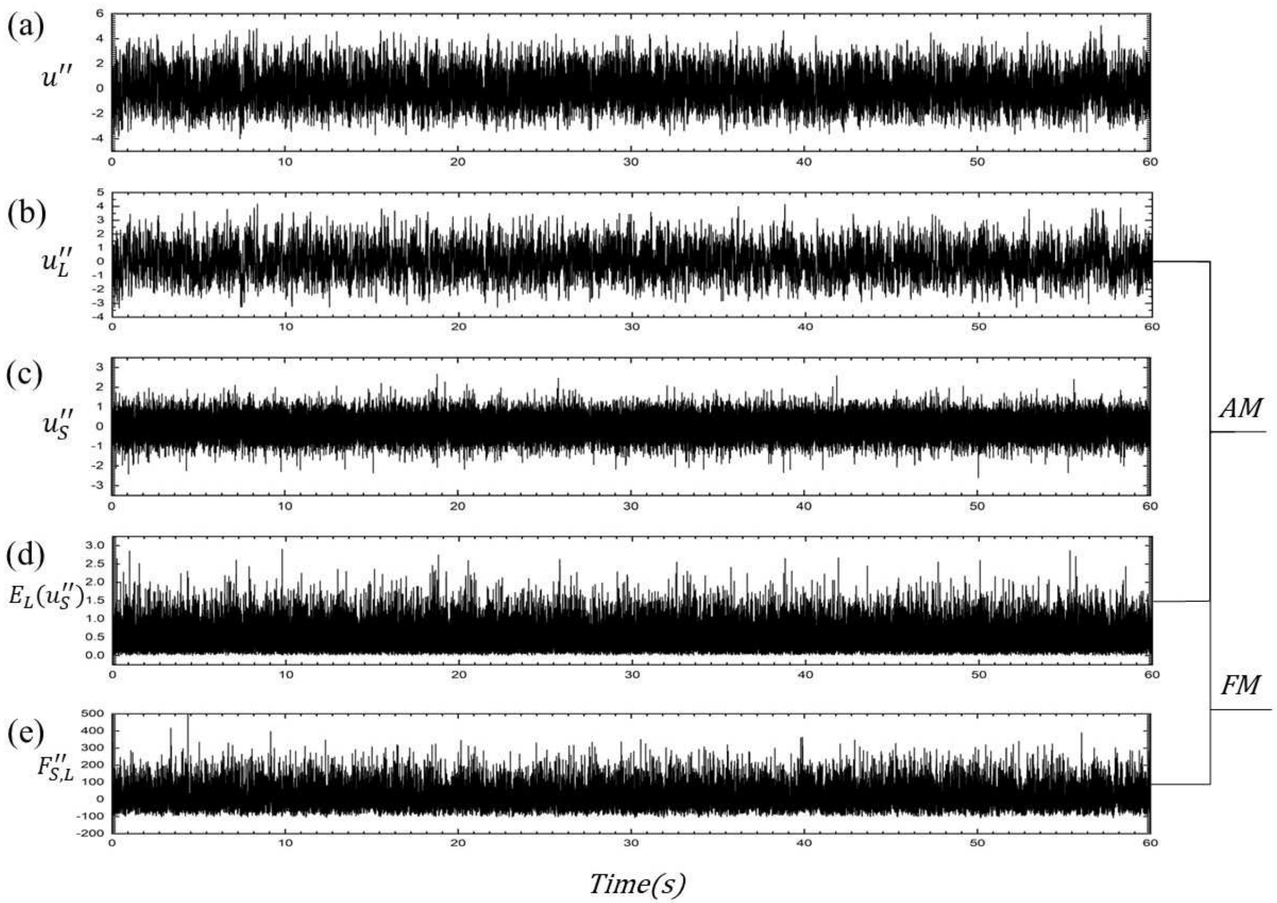

Figure 11. Time series of fluctuating streamwise velocity. (a) Raw data *u''*; (b) large-scale u_L'' and (c) small-scale u_S'' components after filtering; (d) filtered envelope of small-scale components $E_L(u_s'')$; together with (e) large-scale variation of the small-scale frequency $F_{S,L}''$.

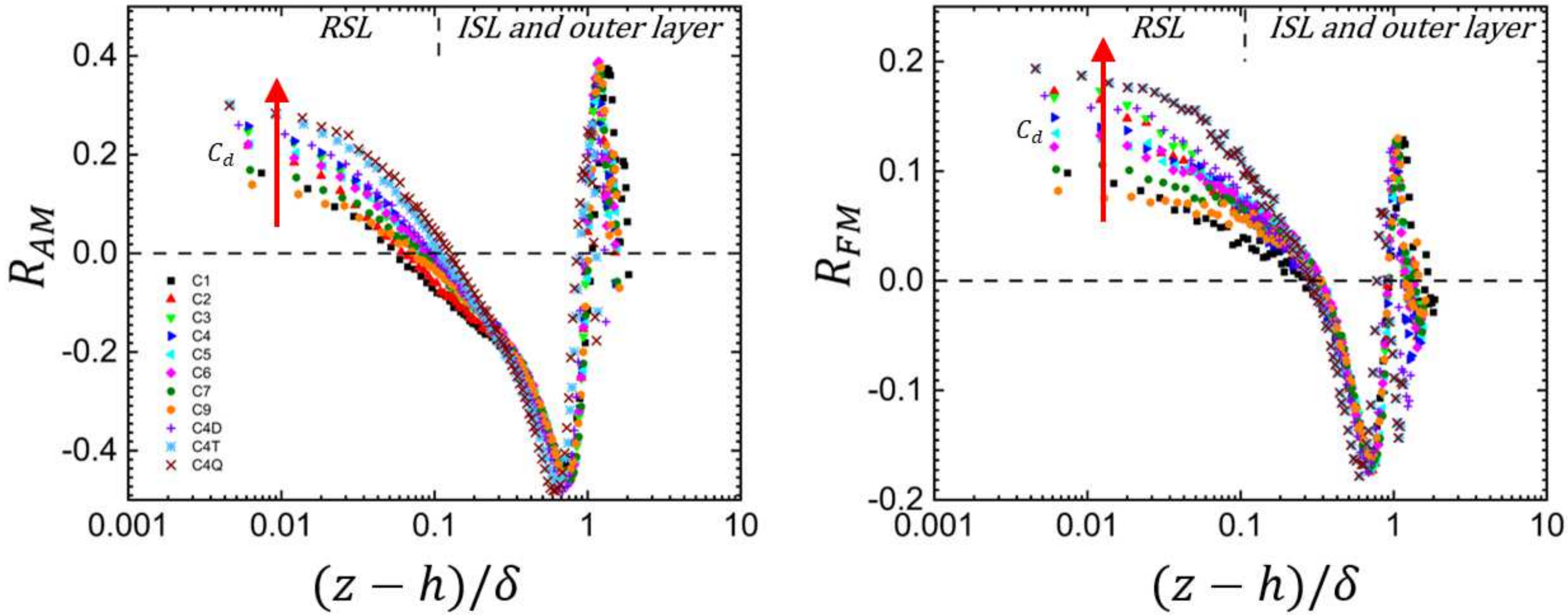

Figure 12. Coefficients of (a) amplitude modulation (AM) R_{AM} (= $\overline{u_L'' E_L(u_S'')} \Big/ \left\{ \left[\overline{u_L''^2} \right]^{1/2} \times \left[\overline{E_L(u_S'')^2} \right]^{1/2} \right\}$) and (b) frequency modulation (FM) R_{FM} (= $\overline{u_L'' F_{S,L}''} \Big/ \left[\left(\overline{u_L''^2} \right)^{1/2} \times \left(\overline{F_{S,L}''^2} \right)^{1/2} \right]$) between the large-scale component u_L'' and the filtered envelope of the small-scale components $E_L(u_S'')$ of streamwise fluctuating velocity u'' over different rough surfaces. Arrow points increasing drag coefficient C_d.

The AM correlation coefficients R_{AM} can be categorized into three different trends over the rough surfaces (Figure 12a). It is positive, elevated in the RSL bottom followed by a gradual decrease with increasing height z, zero-crossing, and finally switches to negative in the ISL. The tight correlation observed in the RSLs in turn suggests that large-scale streamwise fluctuating velocity are positively correlated with small-scale ones. The correlation diminishes (R_{AM} close to zero) around the RSL-ISL interface that is known as *phase reversal* (Chung and McKeon, 2010). In the ISLs, the correlation reverse ($R_{AM} < 0$) in which the large-scale fluctuations are negatively correlated with the small-scale ones. It reaches a negative peak ($R_{AM} \leq -0.4$) in the outer layer ($z - h \geq 0.5\delta$) which is attributed to TBL intermittency (Zhang et al., 2020). In addition, the (high-level, positive) R_{AM} in the RSLs increases with increasing C_d. As such, the AM coupling is enhanced by surface roughness. Besides, the AM correlation coefficients R_{AM} increase approaching the roughness elements that suggest the more significant amplitude modulation between the large and small scales.

Similar to the AM correlation coefficients, the FM correlation coefficients R_{FM} depict the interaction between the signature of small and large scales in the same distribution regime (Figure 12b). Unlike R_{AM}, R_{FM} evidences the positive, high-level correlations in both the RSLs and ISLs. The correlation coefficient R_{FM} diminishes thereover with increasing height in the outer layer ($z - h \geq 0.5\delta$). The strong association of FM between RSL and ISL shows that large-scale fluctuations and small-scale frequency are positively correlated. Whereas, $R_{FM} < 0$, which denotes that large-scale fluctuations are negatively linked with large-scale variation of small-scale frequency, is observed in the outer layer. As a result, both amplitude and frequency of small motion scales in the RSLs are closely influenced by the positive, large-scale streamwise fluctuating velocity. Alike AM, surface roughness amplifies the FM effect.

To further demonstrate the AM, the variance of small-scale streamwise fluctuating velocity $u_S''^2$ is used to quantify the scale interaction as a function of large-scale streamwise fluctuating velocity u_L'' and height z (Figure 13). As shown previously by R_{AM}, there exists a strong modulation between the small- and large-scale streamwise fluctuating velocities in the RSLs $z - h \leq 0.2\delta$ (Ganapathisubramani et al., 2012). Obviously, the variance of small-scale streamwise fluctuating velocity $u_S''^2$ is more energetic in the RSL, overlapping with the positive, large-scale streamwise fluctuating velocity $u_L''/u_\tau \geq 0$ (Figure 13). Moreover, large scale acceleration contributes more, closer to the RSL bottom at faster wind speed, signifying the tight correlation between RSL small and large scales. Whereas, negative, large-scale streamwise deceleration $u_L''/u_\tau < 0$ does not show noticeable correlation. As such, AM is more remarkable during (streamwise) acceleration (but not deceleration), concurring the more energetic sweeps Q4 and entrainment in RSLs reported elsewhere by laboratory experiments (Mo et al., 2022) as well as mathematical models (Yao et al., 2022). Besides, the contribution from u_L'' to $u_S''^2$ is augmented with increasing drag coefficient C_d. In this connection, AM plays a more important role over rougher surfaces. We therefore further hypothesize that large-scale streamwise fluctuating velocity drives its small-scale RSL counterpart, entraining momentum to overcome the aerodynamic resistance. By contrast, large-scale streamwise fluctuating flows u_L''/u_τ do not affect much the small-scale streamwise velocity variance $u_S''^2/u_\tau^2$ in the outer layer.

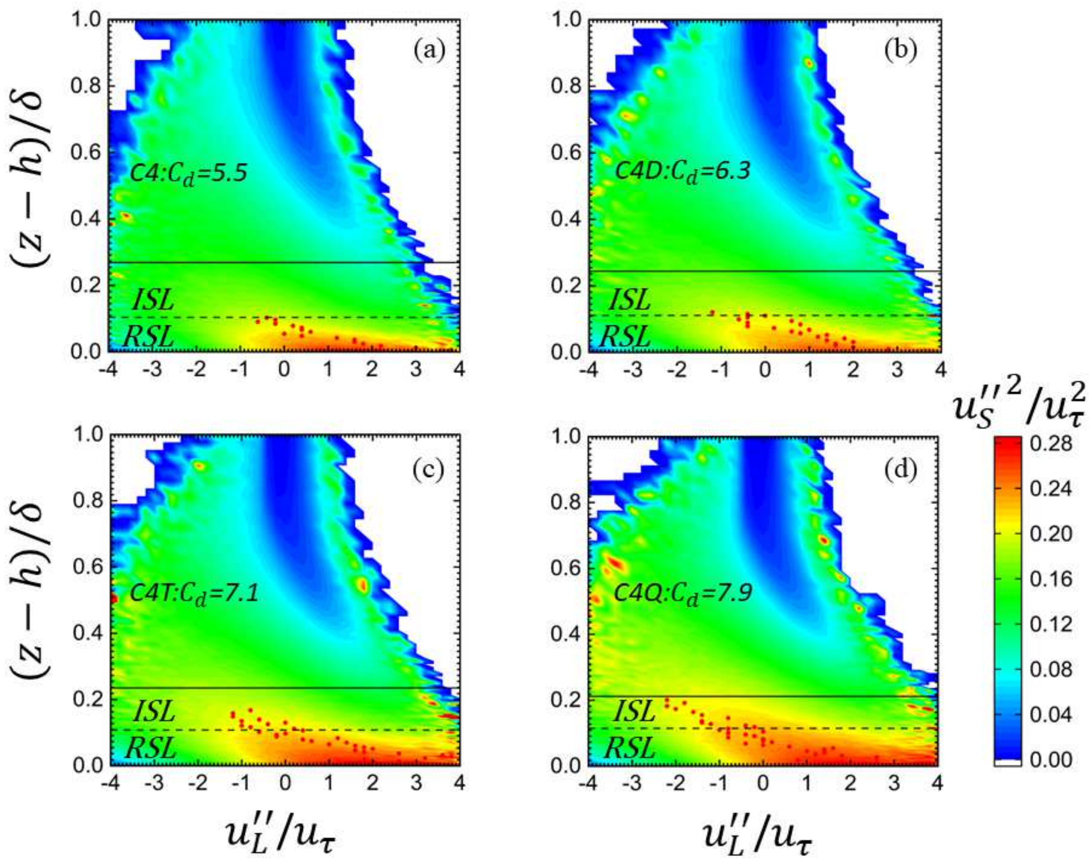

Figure 13. Shaded contours of small-scale streamwise velocity variance $u_S''^2/u_\tau^2$ plotted as a function of large-scale streamwise fluctuating velocity u_L''/u_τ and vertical height z. (a) C4; (b) C4D; (c) C4T; and (d) C4Q. Dashed and solid lines denote the RSL and ISL top, respectively. Red dots indicate the loci of maximum $u_S''^2/u_\tau^2$ at different elevation.

518

4. Practical Significance

To verify the aforementioned hypotheses, Figure 10 shows the TKE production budget

$$P = -\langle \overline{u"w"} \rangle \times \frac{\partial \langle \overline{u} \rangle}{\partial z} \tag{13}$$

and the turbulent TKE flux

$$F_{TKE} = \frac{1}{2} \times \langle \overline{u"u"w"} \rangle + \langle \overline{w"w"w"} \rangle \tag{14}$$

in the space domain as functions of height z over different rough surfaces. As C_d increases, P decreases in the RSL. The difference in TKE production budget between the most and least rough surfaces is up to 50% (Figure 14a). On the contrary, it is negligible in the ISL. Unexpectedly, the lower is the aerodynamic resistance, the more important the TKE production in the RSL.

The vertical TKE flux F_{TKE} concurs Han et al. (2017) that denotes the TKE transfer. Positive and negative vertical TKE flux represent TKE detrainment and entrainment, respectively. All the cases exhibit downward TKE transport ($F_{TKE} < 0$) close to the roughness elements except Cases C1 and C2 with least surface roughness (Figure 14b). Moreover, the TKE entrainment increases significantly with increasing C_d in the RSL. It presents a reverse observation in the ISL so the detrainment (upward TKE flux) decreases with increasing aerodynamic resistance. It is in turn implied that the downward TKE flux is more important to rougher surfaces, entraining energy and momentum from the outer layers through the ISL down to the RSL. These results support our hypothesis that increasing surface roughness leads to decreasing RSL TKE production and a significant increase in TKE entrainment. This finding is consistent with our observations in the cospectrum (Figures 6, 7 and 8). Although the correlation between streamwise and vertical small-scale motion Φ_{uw} diminishes with increasing surface roughness, the RSL transport efficiency η increases due to the (make up of) substantial momentum entrainment.

As postulated by these results, roughness elements play a crucial role in RSL turbulent transport so is vital to street-level ventilation. Analysis of turbulent transport mechanism shows that the presence of roughness elements dominates that enhances the transport efficiency η. Rougher surfaces enhance mixing and transport processes that collectively amplify the modulations between the large and small scales in the RSLs. Furthermore, the RSL TKE entrainment F_{TKE} increases with increasing drag coefficient C_d, constantly inducing fresh air from the outer layers. As a result, roughness elements are beneficial to natural ventilation in urban areas. From a practical point of view, this implies that more favorable street-level ventilation could be realized by loose building arrangement and building height variability (increasing aerodynamic resistance).

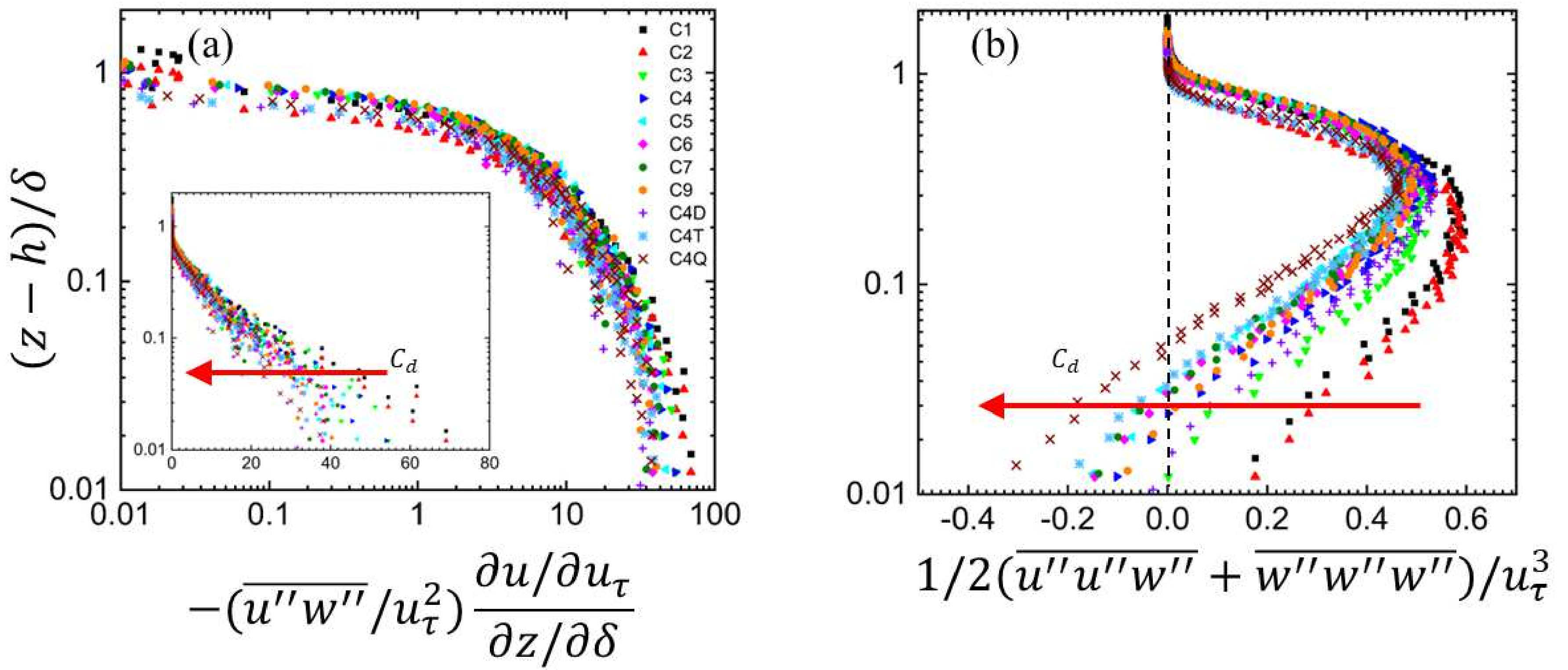

Figure 14. Dimensionless profiles of (a) TKE production budget P (= $-\langle\overline{u''w''}\rangle\times\partial\langle\overline{u}\rangle/\partial z$) and (b) TKE flux F_{TKE} ($F_{TKE}=\left[\langle\overline{u''u''w''}\rangle+\langle\overline{w''w''w''}\rangle\right]/2$) plotted as functions of height z over different rough surfaces. Arrow points increasing drag coefficient C_d.

553

5. Conclusion

This study conducts wind tunnel measurements over idealized urban morphology to elucidate the fundamental city ventilation mechanism. In the street-level ventilation perspective, the RSL, whose dynamics is less homogeneous than those in the ISL, is developed immediately over an array of roughness elements. Besides, it shows a tight correlation with the drag coefficient C_d. Quadrants Qi, and tilt angle Θ, demonstrating the more efficient RSL transport (more uniform mean-wind speeds than its ISL counterpart) than that over smoother surfaces. Our key findings based on turbulence statistics, spectral analysis, and scale interaction are summarized below.

- Turbulence Statistics: Among others, roughness length z_0 increases monotonically with increasing drag coefficient C_d that measures well the aerodynamic resistance of urban areas. While the RSL wind speeds are slowed down over rougher surfaces, the transport efficiency, which is measured by the exuberance η, increases, improving street-level ventilation. Further to quadrant analysis Qi, the tilt angle Θ increases with increasing C_d due to the energetic vertical fluctuating velocity w''.

- Spectral Analysis: While the integral length scale is comparable to the TBL thickness $\Lambda_x \approx \delta$, the RSL eddy size enlarges faster in height over smoother surfaces. Although the spectra of streamwise u'' and vertical w'' fluctuating velocities show no change in TKE in response to RSL small-scale motions ($\lambda_x \leq 0.1\delta$), a substantial increase in the cospectra of vertical momentum flux $u''w''$ is clearly observed.

Hence, surface-mounted roughness elements barely increase the RSL TKE but enhance the correlation between the streamwise and vertical flows throughout the range of motion scales. The tight coupling between the small-scale streamwise and vertical flows in turn enhances the transport processes being driven by the motion scales comparable to the size of the roughness elements.

- Scale interaction: Amplitude (AM) and frequency (FM) modulations indicate that large- and small-scale motions are positively correlated in the RSLs. The coupling between small and large motion scales is tightened by surface roughness. TKE production is more significant in smoother RSLs that is usually assembled by closely packed roughness elements of uniform height. On the other hand, the downward TKE flux, which entrains momentum from the outer layers through the ISL down to the RSL, dominates over rougher surfaces that often consist of loosely packed roughness elements with diversified sizes. This finding suggests that, unexpectedly, the rougher is the aerodynamic resistance, the weaker the (local) TKE production. Instead, rougher urban areas promote entrainment from outer layers through ISLs down to RSLs that is favorable to street-level ventilation.

This study unveils the basic street-level ventilation mechanism and contrasts the forcing of winds and ventilation over sparce (TKE local production) and dense (TKE entrainment) urban areas based on identical, idealized, roughness element. The findings demystify the fundamental mechanism of various existing urban-planning practices, such as packing density, building setback, or air corridors, by a series of systematic fluid mechanics examinations. The outcome would help practitioners to effectuate street-level ventilation by properly architectural design as well as urban planning, utilizing the limited land resource for sustainable cities. Real urban morphology will be adopted in the future to verify the newly developed theory.

Acknowledgment

This study is partly supported by the Hong Kong (HK) Research Grants Council (RGC) RGC Collaborative Research Fund (CRF) C7064-18G, the RGC General Research Fund (GRF) 17209819 and 17211322 as well as the General Programme of Guangdong Natural Science Fund GD-NSF No. 2021A1515012517.

References

Agostini, L., Leschziner, M., 2017. Spectral analysis of near-wall turbulence in channel flow at $Re_{\tau} = 4200$ with emphasis on the attached-eddy hypothesis. Phys. Rev. Fluids 2, 014603. https://doi.org/10.1103/PhysRevFluids.2.014603

Agostini, L., Leschziner, M., 2016. Predicting the response of small-scale near-wall turbulence to large-scale outer motions. Physics of Fluids 28, 015107. https://doi.org/10.1063/1.4939712

Baars, W.J., Talluru, K.M., Hutchins, N., Marusic, I., 2015. Wavelet analysis of wall turbulence to study large-scale modulation of small scales. Exp Fluids 56, 188. https://doi.org/10.1007/s00348-015-2058-8

Barlow, J.F., 2014. Progress in observing and modelling the urban boundary layer. Urban Climate, ICUC8: The 8th International Conference on Urban Climate and the 10th Symposium on the Urban Environment 10, 216–240. https://doi.org/10.1016/j.uclim.2014.03.011

Belcher, S.E., Harman, I.N., Finnigan, J.J., 2012. The Wind in the Willows: Flows in Forest Canopies in Complex Terrain. Annu. Rev. Fluid Mech. 44, 479–504. https://doi.org/10.1146/annurev-fluid-120710-101036

Blackman, K., Perret, L., Calmet, I., Rivet, C., 2017. Turbulent kinetic energy budget in the boundary layer developing over an urban-like rough wall using PIV. Physics of Fluids 29, 085113. https://doi.org/10.1063/1.4997205

Böhm, M., Finnigan, J.J., Raupach, M.R., Hughes, D., 2013. Turbulence Structure Within and Above a Canopy of Bluff Elements. Boundary-Layer Meteorol 146, 393–419. https://doi.org/10.1007/s10546-012-9770-1

Brunet, Y., 2020. Turbulent Flow in Plant Canopies: Historical Perspective and Overview. Boundary-Layer Meteorol 177, 315–364. https://doi.org/10.1007/s10546-020-00560-7

Bruun, H.H., 1971. Interpretation of a hot wire signal using a universal calibration law. J. Phys. E: Sci. Instrum. 4, 225–231. https://doi.org/10.1088/0022-3735/4/3/016

Chen, J.G., Vassilicos, J.C., 2022. Scalings of scale-by-scale turbulence energy in non-homogeneous turbulence. J. Fluid Mech. 938, A7. https://doi.org/10.1017/jfm.2022.153

Cheng, H., Hayden, P., Robins, A.G., Castro, I.P., 2007. Flow over cube arrays of different packing densities. Journal of Wind Engineering and Industrial Aerodynamics 95, 715–740. https://doi.org/10.1016/j.jweia.2007.01.004

Cheng, Y., Li, Q., Argentini, S., Sayde, C., Gentine, P., 2020. A Model for Turbulence Spectra in the Equilibrium Range of the Stable Atmospheric Boundary Layer. J. Geophys. Res. Atmos. 125. https://doi.org/10.1029/2019JD032191

Chin, C.C., Hutchins, N., Ooi, A.S.H., Marusic, I., 2009. Use of direct numerical simulation (DNS) data to investigate spatial resolution issues in measurements of wall-bounded turbulence. Meas. Sci. Technol. 20, 115401. https://doi.org/10.1088/0957-0233/20/11/115401

Christen, A., van Gorsel, E., Vogt, R., 2007. Coherent structures in urban roughness sublayer turbulence. International Journal of Climatology 27, 1955–1968. https://doi.org/10.1002/joc.1625

Conan, B., Aubrun, S., Coudour, B., Chetehouna, K., Garo, J.-P., 2015. Contribution of coherent structures to momentum and concentration fluxes over a flat vegetation canopy modelled in a wind tunnel. Atmospheric Environment 107, 329–341. https://doi.org/10.1016/j.atmosenv.2015.02.061

Demarco, G., Martins, L.G.N., Bodmann, B.E.J., Puhales, F.S., Acevedo, O.C., Wittwer, A.R., Costa, F.D., Roberti, D.R., Loredo-Souza, A.M., Degrazia, F.C., Tirabassi, T., Degrazia, G.A., 2022. Analysis of Thermal and Roughness Effects on the Turbulent Characteristics of Experimentally Simulated Boundary Layers in a Wind Tunnel. IJERPH 19, 5134. https://doi.org/10.3390/ijerph19095134

Dhimal, M., Chirico, F., Bista, B., Sharma, S., Chalise, B., Dhimal, M.L., Ilesanmi, O.S., Trucillo, P., Sofia, D., 2021. Impact of Air Pollution on Global Burden of Disease in 2019. Processes 9, 1719. https://doi.org/10.3390/pr9101719

Finnigan, J.J., Shaw, R.H., 2000. A Wind-Tunnel Study of Airflow in Waving Wheat: An EOF Analysis of the Structure of the Large-Eddy Motion. Boundary-Layer Meteorology 96, 211–255. https://doi.org/10.1023/A:1002618621171

Finnigan, J.J., Shaw, R.H., Patton, E.G., 2009. Turbulence structure above a vegetation canopy. J. Fluid Mech. 637, 387–424. https://doi.org/10.1017/S0022112009990589

Fitzmaurice, L., Shaw, R.H., Paw U, K.T., Patton, E.G., 2004. Three-Dimensional Scalar Microfront Systems in a Large-Eddy Simulation of Vegetation Canopy Flow. Boundary-Layer Meteorology 112, 107–127. https://doi.org/10.1023/B:BOUN.0000020159.98239.4a

Ganapathisubramani, B., Hutchins, N., Monty, J.P., Chung, D., Marusic, I., 2012. Amplitude and frequency modulation in wall turbulence. J. Fluid Mech. 712, 61–91. https://doi.org/10.1017/jfm.2012.398

Hagishima, A., Tanimoto, J., Nagayama, K., Meno, S., 2009. Aerodynamic Parameters of Regular Arrays of Rectangular Blocks with Various Geometries. Boundary-Layer Meteorol 132, 315–337. https://doi.org/10.1007/s10546-009-9403-5

Han, X., He, G., Fang, H., 2017. Double-averaging analysis of turbulent kinetic energy fluxes and budget based on large-eddy simulation. J Hydrodyn 29, 567–574. https://doi.org/10.1016/S1001-6058(16)60769-2

He, B.-J., Ding, L., Prasad, D., 2020. Relationships among local-scale urban morphology, urban ventilation, urban heat island and outdoor thermal comfort under sea breeze influence. Sustainable Cities and Society 60, 102289. https://doi.org/10.1016/j.scs.2020.102289

Hertwig, D., Patnaik, G., Leitl, B., 2017. LES validation of urban flow, part II: eddy statistics and flow structures. Environ Fluid Mech 17, 551–578. https://doi.org/10.1007/s10652-016-9504-x

Ho, Y.-K., Liu, C.-H., 2017a. A wind tunnel study of flows over idealised urban surfaces with roughness sublayer corrections. Theor Appl Climatol 130, 305–320. https://doi.org/10.1007/s00704-016-1877-8

Ho, Y.-K., Liu, C.-H., 2017b. Street-level ventilation in hypothetical urban areas. Atmosphere 8, 124. https:// doi:10.3390/atmos8070124

Iacobello, G., Ridolfi, L., Scarsoglio, S., 2021. Large-to-small scale frequency modulation analysis in wall-bounded turbulence via visibility networks. J. Fluid Mech. 918, A13. https://doi.org/10.1017/jfm.2021.279

Kanda, M., 2006. Large-Eddy Simulations on the Effects of Surface Geometry of Building Arrays on Turbulent Organized Structures. Boundary-Layer Meteorol 118, 151–168. https://doi.org/10.1007/s10546-005-5294-2

Katul, G., Poggi, D., Cava, D., Finnigan, J., 2006. The relative importance of ejections and sweeps to momentum transfer in the atmospheric boundary layer. Boundary-Layer Meteorol 120, 367–375. https://doi.org/10.1007/s10546-006-9064-6

Kolmogorov, A.N., 1991. The Local Structure of Turbulence in Incompressible Viscous Fluid for Very Large Reynolds Numbers. Proceedings: Mathematical and Physical Sciences 434, 9–13.

Lawal, O., Ogugbue, C.J., Imam, T.S., 2023. Mining association rules between lichens and air quality to support urban air quality monitoring in Nigeria. Heliyon 9, e13073. https://doi.org/10.1016/j.heliyon.2023.e13073

Leung, K.K., Liu, C.-H., Wong, C.C.C., Lo, J.C.Y., Ng, G.C.T., 2012. On the study of ventilation and pollutant removal over idealized two-dimensional urban street canyons. Build. Simul. 5, 359–369. https://doi.org/10.1007/s12273-012-0085-4

Li, B., Jiang, C., Wang, L., Liu, J., 2022. Wind tunnel study on influences of morphological parameters on drag coefficient of horizontal non-uniform buildings. Building and Environment 207, 108412. https://doi.org/10.1016/j.buildenv.2021.108412

Liang, M., Chao, Y., Tu, Y., Xu, T., 2023. Vehicle Pollutant Dispersion in the Urban Atmospheric Environment: A Review of Mechanism, Modeling, and Application. Atmosphere 14, 279. https://doi.org/10.3390/atmos14020279

Lim, J., Ooka, R., Lim, H., 2022. Multicollinearity issue for the parameterization of urban ventilation potential with urban morphology. Sustainable Cities and Society 87, 104218. https://doi.org/10.1016/j.scs.2022.104218

Liu, C.-H., Mo, Z., Wu, Z., 2018. Parameterization of vertical dispersion coefficient over idealized rough surfaces in isothermal conditions. Geosci. Lett. 5, 24. https://doi.org/10.1186/s40562-018-0123-x

Liu, C.-H., Ng, C.-T., Wong, C.C.C., 2015. A theory of ventilation estimate over hypothetical urban areas. Journal of Hazardous Materials 296, 9–16. https://doi.org/10.1016/j.jhazmat.2015.04.018

Liu, Y., Liu, C.-H., Brasseur, G.P., Chao, C.Y.H., 2023a. Proper orthogonal decomposition of large-eddy simulation data over real urban morphology. Sustainable Cities and Society 89, 104324. https://doi.org/10.1016/j.scs.2022.104324

Liu, Y., Liu, C.-H., Brasseur, G.P., Chao, C.Y.H., 2023b. Wavelet analysis of the atmospheric flows over real urban morphology. Science of The Total Environment 859, 160209. https://doi.org/10.1016/j.scitotenv.2022.160209

Lumley, J.L., 1964. The Spectrum of Nearly Inertial Turbulence in a Stably Stratified Fluid. Journal of the Atmospheric Sciences 21, 99–102. https://doi.org/10.1175/1520-0469(1964)021<0099:TSONIT>2.0.CO;2

Mäteling, E., Klaas, M., Schröder, W., 2020. Detection of small-scale/large-scale interactions in turbulent wall-bounded flows. Phys. Rev. Fluids 5, 114610. https://doi.org/10.1103/PhysRevFluids.5.114610

Michioka, T., Funaki, R., Kawai, T., 2023. Effects of Building Arrays on Large-Scale Turbulent Motions Within an Urban Canopy. Boundary-Layer Meteorol. https://doi.org/10.1007/s10546-022-00778-7

Michioka, T., Sato, A., Takimoto, H., Kanda, M., 2011. Large-Eddy Simulation for the Mechanism of Pollutant Removal from a Two-Dimensional Street Canyon. Boundary-Layer Meteorol 138, 195–213. https://doi.org/10.1007/s10546-010-9556-2

Mo, Z., Liu, C.-H., 2023. Inertial and roughness sublayer flows over real urban morphology: A comparison of wind tunnel experiment and large-eddy simulation. Urban Climate 49, 101530. https://doi.org/10.1016/j.uclim.2023.101530

Mo, Z., Liu, C.-H., 2019. Transport mechanism of urban plume dispersion. Building and Environment 161, 106239. https://doi.org/10.1016/j.buildenv.2019.106239

Mo, Z., Liu, C.-H., 2018a. Wind tunnel measurements of pollutant plume dispersion over hypothetical urban areas. Building and Environment 132, 357–366. https://doi.org/10.1016/j.buildenv.2018.01.046

Mo, Z., Liu, C.-H., 2018b. A wind tunnel study of ventilation mechanism over hypothetical urban roughness: The role of intermittent motion scales. Building and Environment 135, 94–103. https://doi.org/10.1016/j.buildenv.2018.02.031

Mo, Z., Liu, C.-H., 2018c. Wind tunnel measurements of turbulent boundary layer flows over arrays of ribs and cubes. Geosci. Lett. 5, 16. https://doi.org/10.1186/s40562-018-0115-x

Mo, Z., Liu, C.-H., Chow, H.-L., Lam, M.-K., Lok, Y.-H., Ma, S.-W., Wong, F.-L., Yip, P.-Y., 2022. Roughness sublayer over vegetation canopy: A wind tunnel study. Agricultural and Forest Meteorology 316, 108880. https://doi.org/10.1016/j.agrformet.2022.108880

Mo, Z., Liu, C.-H., Ho, Y.-K., 2021. Roughness sublayer flows over real urban morphology: A wind tunnel study. Building and Environment 188, 107463. https://doi.org/10.1016/j.buildenv.2020.107463

Palusci, O., Monti, P., Cecere, C., Montazeri, H., Blocken, B., 2022. Impact of morphological parameters on urban ventilation in compact cities: The case of the Tuscolano-Don

Bosco district in Rome. Science of The Total Environment 807, 150490. https://doi.org/10.1016/j.scitotenv.2021.150490

Pathikonda, G., Christensen, K.T., 2017. Inner–outer interactions in a turbulent boundary layer overlying complex roughness. Phys. Rev. Fluids 2, 044603. https://doi.org/10.1103/PhysRevFluids.2.044603

Peng, Y., Gao, Z., Buccolieri, R., Shen, J., Ding, W., 2021. Urban ventilation of typical residential streets and impact of building form variation. Sustainable Cities and Society 67, 102735. https://doi.org/10.1016/j.scs.2021.102735

Peng, Z., Sun, J., 2014. Characteristics of the Drag Coefficient in the Roughness Sublayer over a Complex Urban Surface. Boundary-Layer Meteorol 153, 569–580. https://doi.org/10.1007/s10546-014-9949-8

Perret, L., Kerhervé, F., 2019. Identification of very large scale structures in the boundary layer over large roughness elements. Exp Fluids 60, 97. https://doi.org/10.1007/s00348-019-2749-7

Raupach, M.R., Antonia, R.A., Rajagopalan, S., 1991. Rough-wall turbulent boundary layers 44.

Roth, M., Inagaki, A., Sugawara, H., Kanda, M., 2015. Small-scale spatial variability of turbulence statistics, (co)spectra and turbulent kinetic energy measured over a regular array of cube roughness. Environ Fluid Mech 15, 329–348. https://doi.org/10.1007/s10652-013-9322-3

Shafi, H.S., Antonia, R.A., 1997. Small-scale characteristics of a turbulent boundary layer over a rough wall. J. Fluid Mech. 342, 263–293. https://doi.org/10.1017/S0022112097005612

Shao, X., Zhang, N., Peng, Z., Zhao, K., Luo, Y., Song, X., 2022. Observed Surface Drag Coefficient Under High Wind Speed Conditions and the Relationship With Coherent Structures. Journal of Geophysical Research: Atmospheres 127, e2021JD035301. https://doi.org/10.1029/2021JD035301

Shaw, R.H., Tavangar, J., Ward, D.P., 1983. Structure of the Reynolds Stress in a Canopy Layer. J. Climate Appl. Meteor. 22, 1922–1931. https://doi.org/10.1175/1520-0450(1983)022<1922:SOTRSI>2.0.CO;2

Tang, Z., Jiang, N., Zheng, X., Wu, Y., 2016. Bursting process of large- and small-scale structures in turbulent boundary layer perturbed by a cylinder roughness element. Exp Fluids 57, 79. https://doi.org/10.1007/s00348-016-2174-0

Vidanapathirana, M., Perera, N., Emmanuel, R., Coorey, S., 2023. Air pollutant dispersion around high-rise building cluster forms: the case of Port City, Colombo, Sri Lank. https://doi.org/10.21203/rs.3.rs-2456185/v1

Wei, W., Schmitt, F.G., Huang, Y.X., Zhang, H.S., 2016. The Analyses of Turbulence Characteristics in the Atmospheric Surface Layer Using Arbitrary-Order Hilbert Spectra. Boundary-Layer Meteorol 159, 391–406. https://doi.org/10.1007/s10546-015-0122-9

Yao, L., Liu, C.-H., Mo, Z., Cheng, W.-C., Brasseur, G.P., Chao, C.Y.H., 2022. Statistical analysis of the organized turbulence structure in the inertial and roughness sublayers over real urban area by building-resolved large-eddy simulation. Building and Environment 207, 108464. https://doi.org/10.1016/j.buildenv.2021.108464

Yoshida, T., Takemi, T., Horiguchi, M., 2018. Large-Eddy-Simulation Study of the Effects of Building-Height Variability on Turbulent Flows over an Actual Urban Area. Boundary-Layer Meteorol 168, 127–153. https://doi.org/10.1007/s10546-018-0344-8

Yuan, J., Aghaei Jouybari, M., 2018. Topographical effects of roughness on turbulence statistics in roughness sublayer. Phys. Rev. Fluids 3, 114603. https://doi.org/10.1103/PhysRevFluids.3.114603

Zaki, S.A., Hagishima, A., Tanimoto, J., Ikegaya, N., 2011. Aerodynamic Parameters of Urban Building Arrays with Random Geometries. Boundary-Layer Meteorol 138, 99–120. https://doi.org/10.1007/s10546-010-9551-7

Zhang, A., Xia, C., Li, W., 2022. Exploring the effects of 3D urban form on urban air quality: Evidence from fifteen megacities in China. Sustainable Cities and Society 78, 103649. https://doi.org/10.1016/j.scs.2021.103649

Zhang, Z.-L., Zhang, M.-M., Cai, C., Cheng, Y., 2020. Characteristics of large- and small-scale structures in the turbulent boundary layer over a drag-reducing riblet surface. Proceedings of the Institution of Mechanical Engineers, Part C: Journal of Mechanical Engineering Science 234, 796–807. https://doi.org/10.1177/0954406219887774